

# TAE: A Model-Constrained Tikhonov Autoencoder Approach for Forward and Inverse Problems <sup>\*</sup>

Hai Van Nguyen <sup>†</sup> and Tan Bui-Thanh <sup>†‡</sup>

**Abstract.** Efficient real-time solvers for forward and inverse problems are essential in engineering and science applications. Machine learning surrogate models have emerged as promising alternatives to traditional methods, offering substantially reduced computational time. Nevertheless, these models typically demand extensive training datasets to achieve robust generalization across diverse scenarios. While physics-based approaches can partially mitigate this data dependency and ensure physics-interpretable solutions, addressing scarce data regimes remains a challenge. Both purely data-driven and physics-based machine learning approaches demonstrate severe overfitting issues when trained with insufficient data. *We propose a novel Tikhonov autoencoder model-constrained framework, called TAE, capable of learning both forward and inverse surrogate models using a single arbitrary observation sample.* We develop comprehensive theoretical foundations including forward and inverse inference error bounds for the proposed approach for linear cases. For comparative analysis, we derive equivalent formulations for pure data-driven and model-constrained approach counterparts. At the heart of our approach is a data randomization strategy, which functions as a generative mechanism for exploring the training data space, enabling effective training of both forward and inverse surrogate models from a single observation, while regularizing the learning process. We validate our approach through extensive numerical experiments on two challenging inverse problems: 2D heat conductivity inversion and initial condition reconstruction for time-dependent 2D Navier–Stokes equations. Results demonstrate that TAE achieves accuracy comparable to traditional Tikhonov solvers and numerical forward solvers for both inverse and forward problems, respectively, while delivering orders of magnitude computational speedups.

**Key words.** Forward problem, inverse problem, randomization, model-constrained, autoencoder, deep learning, deep neural network, partial differential equations.

REQUIRED **AMS subject classifications.** 68Q25, 68R10, 68U05

**1. Introduction.** Partial differential equations (PDEs) serve as the mathematical foundation for describing physical phenomena in science and engineering applications [78, 31]. Generally, these equations lack analytical solutions except in limited special cases, necessitating numerical approaches such as finite difference [65, 26, 60], finite element [69, 71], and finite volume methods [20, 43]. These computational techniques, while essential, often impose significant computational burden, particularly for high-dimensional problems. In this context, PDE-constrained inverse problems represent pervasive mathematical methods in inferring knowledge from experimental and observational data by leveraging numerical simulations and models [38, 64, 83, 80]. Among various methodologies, the Tikhonov regularization framework stands as a predominant approach for addressing general inverse problems [33, 92, 54, 28]. This optimization-based methodology necessitates multiple evaluations of the forward model,

<sup>\*</sup>This research is partially funded by the National Science Foundation awards NSF-OAC-2212442, NSF-2108320, NSF-1808576 and NSF-CAREER-1845799; by the Department of Energy award DE-SC0018147 and DE-SC0022211.

<sup>†</sup>Department of Aerospace Engineering and Engineering Mechanics, the University of Texas at Austin, Texas

<sup>‡</sup>The Oden Institute for Computational Engineering and Sciences, the University of Texas at Austin, Texas ([tanbui@oden.utexas.edu](mailto:tanbui@oden.utexas.edu), <https://users.oden.utexas.edu/~tanbui/>).

which is typically governed by PDEs. Consequently, PDE-constrained inverse problems face two primary challenges: they not only demand substantial computational resources, but also require extensive processing time to obtain solutions, making them impractical for applications requiring real-time responses.

Machine learning has demonstrated remarkable success across diverse domains, from computer vision and natural language processing [40, 18, 82] to physics-based applications including experimental design [76, 12] and digital twins [53, 70, 4]. The autoencoder architecture has emerged as a versatile framework for applications in image processing tasks such as denoising and inpainting [11, 29, 32], as well as in transformer-based natural language processing systems [82]. In science and engineering applications, machine learning approaches have demonstrated significant potential in developing computationally efficient surrogate models for both forward and inverse problems [68, 61, 58, 81, 55, 46, 49]. Traditional data-driven learning methodologies, which construct surrogate models without incorporating physical principles [87, 3], face several limitations. These include the requirement for extensive training datasets to achieve accurate forward or inverse surrogate models [44, 50, 1, 62, 87], limited generalization capabilities, and generating non-physical solutions. To address these challenges, physics-based machine learning approaches have been developed, integrating governing physical principles into the learning framework [68, 59, 56, 21]. However, as noted in [56], these physics-based approaches remain susceptible to overfitting when training data are scarce. The acquisition of comprehensive training datasets presents significant challenges in many engineering applications due to prohibitive costs or practical limitations. For instance, in full wave-form inversion, data collection is constrained by the substantial expenses associated with sensor placement (such as multi-million dollar oil well drilling operations) or accessibility challenges in certain environments (like deep ocean floors). This underscores the critical need for developing machine learning methodologies capable of constructing physics-interpretable surrogate models from minimal training samples.

Physics-informed neural networks (PINNs) [68] employ neural networks to parametrize solutions for both PDEs [68, 85, 10] and PDE-constrained inverse problems [68, 34, 35, 14], using spatial or temporal variables as inputs. The neural network parameters are optimized through objective functions comprising multiple loss terms, including PDE constraints, boundary conditions, initial conditions, and observation data misfits. An alternative approach, aligned with the concept of neural fields [88], has emerged in inverse problem solving [79, 77, 21, 6]. This methodology processes neural network inverted solutions through numerical forward simulations to generate synthetic data, which is then reconciled with observational data to optimize the neural representation of solutions. While these approaches offer the advantage of mesh-independent solutions—capable of producing results at any spatiotemporal point post-training—they suffer from a significant limitation: the requirement to retrain the network for each new scenario, including variations in model parameters, boundary conditions, or observation sets. As such, these methods do not have the ability to generalize to unseen inference cases, which are critical requirement for making physics-based machine learning surrogate models viable in real-time applications. Furthermore, research has shown that PINNs demand extensive training periods and numerous architectural experiments to achieve adequate solution convergence [17]. This limitation becomes particularly problematic in inverse problems, in which the PDE must be solved repeatedly throughout optimization iterations.

Alternative approaches proposed in [73, 91] focus on learning regularizer functions for inverse problems from extensive training datasets. While these learned neural network regularizers enhance solution quality compared to traditional Tikhonov regularization, they essentially represent another computationally intensive method for solving PDEs or PDE-constrained inverse problems, making them unsuitable for real-time applications.

Various methodologies have emerged for learning parameter-to-observation maps, or more general, numerical PDE simulations, focusing on predicting solution for unseen scenarios from historical snapshots of solutions. Neural ODE [13] and related approaches [81, 86, 55, 93] propose learning the right-hand side of semi-discretized equations, offering the distinctive advantage of predicting solutions at arbitrary temporal points through time integration schemes. Alternative frameworks employ recurrent neural network architectures [41, 24, 52] or transformer-based models [25, 45] to process sequences of historical solution snapshots for future state predictions. These methods, however, are usually constrained by the requirement of uniform temporal sampling for both input and predicted solutions. Another promising direction involves learning dynamics in latent space, where solutions are projected into lower-dimensional representations using autoencoder-like architectures [89, 84, 30, 37, 42] or graph pooling techniques [5, 66]. In these approaches, neural networks are employed to approximate the evolution of the system in the compressed latent space. The operator learning approach [46, 49] potentially offers computationally efficient surrogate models by directly learning functional mappings between parameter fields and target solutions across the physical domain. While all these methodologies demonstrate considerable promise in capturing PDE system dynamics and generating future solution predictions, they generally require substantially large training data to develop accurate surrogate forward models or functional mapping operators.

A variety of machine learning approaches have been developed to create generalizable inverse solvers for PDE-constrained inverse problems. Several researchers [36, 56, 62] have introduced methods that directly regularize neural network inverse surrogate models through differentiable PDE solvers. In these approaches, the predicted Parameters of Interest (PoI) from neural networks are processed through PDE solvers to regenerate synthetic observation data, which is expected to match training observation input data. These physics-based methods demonstrate significant improvements over pure data-driven approaches given equivalent training data volumes. However, the training data requirements for effective inverse mappings correlate with the non-linearity of the parameter-to-observables (PtO) map, making them inherently problem-specific. Our previous research [56] introduced the model-constrained **TNet** approach for learning Tikhonov inverse solvers from a finite training dataset. Notably, with identical sample sizes, both pure machine learning and physics-based approaches face overfitting challenges compared to **TNet**. Related work [48, 36] proposes first training the forward map to learn the PDE solver, which then constrains the inverse map learning process with pre-trained PDE surrogate models, thereby reducing overall training costs. Alternative approaches [15, 8] employ dual autoencoder architectures to compress both observation and PoI data spaces into lower-dimensional latent representations, followed by learning linear inverse mappings between these compressed spaces. Additionally, variational autoencoder architectures have been widely adopted for probabilistic inverse problem solving [27, 2]. Some efforts [27] focus on simultaneous learning of forward and inverse surrogate models. However, in this work, concurrent training of encoders and decoders for both forward and inverse map-

plings can complicate training convergence due to the increased dimensionality of the trainable parameter space, and the competition between the encoder and the decoder.

In scientific machine learning, enhancing surrogate model generalization remains a critical objective and a grand challenge. Several researchers [63, 90, 19, 74, 23] have proposed incorporating input-gradient information into the loss function to improve neural network solution accuracy and generalization capabilities. However, the computational cost of explicitly computing Jacobian matrices through back-propagation for optimization is substantial, particularly for high-dimensional input problems, due to the requirement for double back-propagation. While [58] demonstrates that exploiting low-rank properties of Jacobian matrices can reduce computational overhead, our previous work [55, 56] shows that comparable regularization effects can be achieved through data randomization techniques in forward surrogate model learning. This randomization approach, which introduces controlled noise to neural network input data, has been shown to enhance long-term predictive stability [75, 67, 55]. Theoretical foundations established in [72, 7, 51] demonstrate that input data perturbation effectively functions as Tikhonov regularization, promoting input-space smoothness in neural network responses. Our recent work [56, 55] show that randomization induces regularization on the derivatives without actually computing them (which we try to avoid due to the aforementioned reasons). Our works further validate that data randomization not only improves the generalization capability of learned inverse surrogate models to unseen observation scenarios but also substantially reduces training data requirements.

This paper extends our previous research [56] by introducing **TAE**, a Tikhonov autoencoder model-constrained learning framework **capable of addressing both forward and inverse problems using only a single arbitrary observational sample**. For comparative analysis, we examine various autoencoder architectures, including pure data-driven approaches [87] and model-constrained methods [62, 21, 36]. Our theoretical analysis provides forward and inverse solution error estimates across all approaches for linear problems. These derivations, combined with numerical evidence, suggest that both pure data-driven and model-constrained approaches may yield suboptimal learning strategies for inverse problems due to potential training data bias. In contrast, **TAE** employs data randomization techniques with just one arbitrary observational sample to learn Tikhonov inverse solutions. For linear inverse problems, the approach successfully recovers Tikhonov-regularized solutions while maintaining exact compliance with governing equations at training points. Furthermore, given the pre-trained inverse map encoder and the same observation sample, the decoder accurately represents the forward map/parameter to observable (PtO) mapping for linear problems. We also provide theoretical justification for sequential encoder-decoder training rather than simultaneous optimization. The effectiveness of our proposed approach is demonstrated through extensive numerical experiments on two challenging applications: 2D inverse heat conductivity inversion and initial condition reconstruction for time-dependent 2D Navier–Stokes equations.

There are several limitations to our approaches. The primary constraint stems from the requirement for a differentiable solver, which results in training and memory costs that scale with multiple forward solution computations. One potential solution, as demonstrated in [36], is to learn surrogate models for PDEs before incorporating them into **TAE** framework. A second limitation arises from **TAE**'s design principle: learn the Tikhonov inverse solver and the forward solver at the same time. While it offers improved interpretability and accuracy

compared to purely data-driven approaches, its inverse performance is inherently bounded by the traditional Tikhonov method. Consequently, for scenarios with abundant data, alternative approaches such as [50, 1, 44] may achieve superior accuracy relative to traditional Tikhonov methods, though these alternatives cannot provide real-time inverse solutions as TAE does. Finally, while TAE offers an advantage over existing deep neural network approaches by deriving its regularization parameter directly from the Tikhonov framework—rather than lacking a principled parameter selection method—the challenge of determining optimal regularization parameters remains, just like any approach in finding optimal regularization parameter. This optimization task is highly problem-dependent and computationally extensive.

The paper’s organization is as follows. [Subsection 2.1](#) establishes the fundamental framework of linear and nonlinear PDEs and PDE-constrained inverse problems, along with notational conventions. [Subsection 2.2](#) examines data-driven autoencoder machine learning approaches, specifically nPOP and nOPO. [Subsection 2.3](#) explores model-constrained autoencoder machine learning approaches—mcPOP, mcOPO, and mcOPO-Full—which learn inverse and forward mappings while incorporating model constraints from the parameter-to-observable map of the discretized PDE. In [Subsection 2.4](#), we introduce Tikhonov autoencoder neural networks, TAE and its variant TAE-Full, designed to learn Tikhonov solver and PtO/forward maps while eliminating unnecessary training biases. [Subsection 2.5](#) provides a detailed analysis comparing sequential versus simultaneous training strategies for encoder and decoder networks. [Section 3](#) presents comprehensive numerical experiments validating our theoretical developments through applications to 2D inverse heat conductivity problems and inverse initial conditions for 2D time-dependent Navier-Stokes equations. The paper concludes in [Section 4](#) with future research directions, while detailed proofs of theoretical results are provided in [Section 5](#).

## 2. Methodology.

**2.1. Problem setting and notation.** In this research, we explore various auto-encoder approaches for learning the following functions: the parameter-to-observable (PtO) map or forward map (transforming PoIs to PDE solutions), and inverse mappings (converting observables to PoIs). Our investigation encompasses naïve machine learning approaches ([Subsection 2.2](#)), model-constrained machine learning techniques ([Subsection 2.3](#)), and Tikhonov model-constrained machine learning strategies ([Subsection 2.4](#)). We deviate from traditional concurrent encoder-decoder training by implementing a sequential approach—first training the encoder network, then optimizing the decoder using the pre-trained encoder. The comparative merits of sequential versus simultaneous training are analyzed in [Subsection 2.5](#). Our notation follows standard conventions: matrices are denoted by capital letters, vectors by boldface normal letters, and scalars by lowercase Roman letters. We seek to learn the forward map  $\mathcal{G} : \mathbb{R}^n \mapsto \mathbb{R}^p$  governed by a PDE:

$$(2.1) \quad \boldsymbol{\omega} = \mathcal{G}(\mathbf{u}),$$

or its corresponding parameter-to-observable (PtO) map:

$$(2.2) \quad \mathbf{y} = B \circ \mathcal{G}(\mathbf{u}) + \boldsymbol{\eta} = B\boldsymbol{\omega} + \boldsymbol{\eta},$$

where  $\boldsymbol{\eta}$  represents observation noise,  $\mathbf{u} \in \mathbb{R}^n$  denotes the parameter of interest (PoI),<sup>1</sup>  $\boldsymbol{\omega} \in \mathbb{R}^p$  represents the PDE solution,  $B : \mathbb{R}^p \mapsto \mathbb{R}^m$  defines the observation operator, and  $\mathbf{y} \in \mathbb{R}^m$  represents the observation. For inverse problems, we aim to learn the mapping:

$$(2.3) \quad \mathbf{u} = (B \circ \mathcal{G})^{-1}(\mathbf{y}).$$

Note that the inverse map is not well-defined in general. As we shall show, we learn regularized inverse maps instead.

For clarity in our derivations, we define the following notations: Training data matrices  $U \in \mathbb{R}^{n \times n_t}$  and  $Y \in \mathbb{R}^{m \times n_t}$  contain  $n_t$  PoI samples and  $n_t$  observation samples, respectively. For linear problems,  $G$  represents the linear forward map, while  $G^B = B \circ G$  denotes its corresponding linear PtO map. Neural network components  $\Psi_e$  and  $\Psi_d$  represent encoder and decoder networks, respectively. In linear neural networks,  $\{W_e, \mathbf{b}_e\}$  and  $\{W_d, \mathbf{b}_d\}$  denote weight matrices and bias vectors for encoder and decoder networks, respectively. We define additional notations:  $\bar{\mathbf{x}} = X \frac{\mathbf{1}}{n_t}$  computes the column mean of matrix  $X$ ,  $\bar{X} = X - \bar{\mathbf{x}}\mathbf{1}^T$  represents the centered-column matrix,  $\mathbf{1}$  denotes a column vector of ones, while  $\|\cdot\|_F$  indicates the Frobenius norm and  $\dagger$  denotes matrix pseudo-inverse.

**2.2. Naïve autoencoder learning approaches.** In this section, we present two naive data-driven autoencoder approaches that are commonly employed for learning PtO and inverse mappings in engineering applications. These approaches rely exclusively on training data pairs  $\{U, Y\}$  without incorporating any physical models or domain knowledge into their loss functions [27, 15, 87, 3].

**2.2.1. Naive autoencoder PtO-inverse learning approach nPOP.** In this approach, we learn the encoder for PtO map and the decoder for inverse map. Given the training data set  $\{U, Y\}$ , the loss functions are defined as

$$(nPOP) \quad \begin{aligned} \Psi_e^* &= \min_{\Psi_e} \frac{1}{2} \|\Psi_e(U) - Y\|_F^2, \\ \Psi_d^* &= \min_{\Psi_d} \frac{1}{2} \|\Psi_d(\Psi_e^*(U)) - U\|_F^2. \end{aligned}$$

For analytical insights, we examine a noise-free linear inverse problem using linear neural networks. The linear encoder learns the PtO map as  $Z = \Psi_e(U) = W_e U + \mathbf{b}_e \mathbf{1}^T$ , while the linear decoder learns the inverse map  $\Psi_d(Z) = W_d Z + \mathbf{b}_d \mathbf{1}^T$ . The first-order optimality conditions yield the following optimal solutions (see the complete derivation in Subsection 5.2):

$$(2.4) \quad \begin{aligned} W_e^* &= G^B \bar{U} \bar{U}^\dagger, & \mathbf{b}_e^* &= G^B (I - \bar{U} \bar{U}^\dagger) \bar{\mathbf{u}}, \\ W_d^* &= \bar{U} \bar{Y}^\dagger, & \mathbf{b}_d^* &= \bar{\mathbf{u}} - \bar{U} \bar{Y}^\dagger \bar{\mathbf{y}}. \end{aligned}$$

It can be seen that if a sufficient number of training data samples are provided such that  $\bar{U}$  is a full row rank matrix, i.e.  $\bar{U} \bar{U}^\dagger = I$ , then the encoder is able to represent exactly the PtO map  $G^B$ , i.e.,  $\Psi_e^*(\mathbf{u}^{\text{test}}) = G^B \mathbf{u}^{\text{test}} = \mathbf{y}^{\text{test}}$ . In other words, the predicted PtO error

---

<sup>1</sup>The parameter vector could be a discrete representation of some distributed parameter field.

estimation is zero,  $\epsilon_{\mathbf{y}^{\text{test}}}^{\text{nPOP}} = 0$ . At the same time, the decoder is able to represent the right inverse of  $G^B$ . Indeed, given a test PoI sample  $\mathbf{y}^{\text{test}}$ , we have

$$(2.5) \quad G^B \Psi_d^* (\mathbf{y}^{\text{test}}) = G^B (W_d^* \mathbf{y}^{\text{test}} + \mathbf{b}_d^*) = G^B \bar{U} \bar{Y}^\dagger \mathbf{y}^{\text{test}} + G^B \bar{\mathbf{u}} - G^B \bar{U} \bar{Y}^\dagger \bar{\mathbf{y}} = I \mathbf{y}^{\text{test}}.$$

It is important to note that the right inverse of  $G^B$  is not unique. In our **nPOP** approach, the decoder is concurrently satisfied with the following identity

$$(\Psi_d^* (Y) - U) Y^T = 0.$$

This identity indicates that the misfit of inverse solutions on training data is orthogonal to the column space of  $\bar{Y}$ . Additionally, it also implies the data-dependent nature (or data-driven property) of the decoder. On the other hand, the decoder is not guaranteed to be the left inverse of  $G^B$ , i.e., the inverted solution error can be written as

$$(2.6) \quad \epsilon_{\mathbf{u}^{\text{test}}}^{\text{nPOP}} = \|\Psi_d^* (\mathbf{y}^{\text{test}}) - \mathbf{u}^{\text{test}}\|_2^2 = \left\| \left( \bar{U} \bar{Y}^\dagger G^B - I \right) (\mathbf{u}^{\text{test}} - \bar{\mathbf{u}}) \right\|_2^2.$$

In the ideal case, we expect **nPOP** to learn the unique left inverse of  $G^B$ , namely,  $(G^B)^\dagger$ , which is the best inverse map in the sense of solving least squares on the test sample. In that case, the error of inverse solutions reads

$$\left\| (G^B)^\dagger \mathbf{y}^{\text{test}} - \mathbf{u}^{\text{test}} \right\|_2^2 = \left\| \left( (G^B)^\dagger G^B - I \right) \mathbf{u}^{\text{test}} \right\|_2^2.$$

It is worth noting that, although we can achieve full row rank matrices  $\bar{U}, \bar{Y}$  by data randomization technique [22], the inverse solution error Equation (2.6) can be very large.

**2.2.2. Naive autoencoder inverse-PtO learning approach nOPO.** In contrast to the **nPOP** approach, we propose the **nOPO** approach that learns inverse map with encoder and PtO map with decoder. The loss functions for **nOPO** are defined as

$$(2.7) \quad \begin{aligned} \Psi_e^* &= \min \frac{1}{2} \|\Psi_e (Y) - U\|_F^2, \\ \Psi_d^* &= \min_{\Psi_d} \frac{1}{2} \|\Psi_d (\Psi_e^* (Y)) - Y\|_F^2. \end{aligned}$$

For insights on **nOPO**, we analyze linear problems using a linear encoder for the inverse map  $Z = \Psi_e (Y) = W_e Y + \mathbf{b}_e \mathbf{1}^T$  and a linear decoder for learning PtO map  $\Psi_d (Z) = W_d Z + \mathbf{b}_d \mathbf{1}^T$ . Substituting into **nOPO** in loss functions, we have

$$(2.7) \quad \begin{aligned} W_e^*, \mathbf{b}_e^* &= \min_{W_e, \mathbf{b}_e} \frac{1}{2} \|W_e Y + \mathbf{b}_e \mathbf{1}^T - U\|_F^2, \\ W_d^*, \mathbf{b}_d^* &= \min_{W_d, \mathbf{b}_d} \frac{1}{2} \|W_d (W_e^* Y + \mathbf{b}_e^* \mathbf{1}^T) + \mathbf{b}_d \mathbf{1}^T - Y\|_F^2. \end{aligned}$$

By applying the first optimality condition, the optimal solutions for (2.7) (see subsection 5.1 for full derivations) are

$$(2.8) \quad \begin{aligned} W_e^* &= \bar{U}\bar{Y}^\dagger, & \mathbf{b}_e^* &= \bar{\mathbf{u}} - \bar{U}\bar{Y}^\dagger\bar{\mathbf{y}}, \\ W_d^* &= \bar{Y}\bar{Z}^\dagger, & \mathbf{b}_d^* &= \bar{\mathbf{y}} - \bar{Y}\bar{Z}^\dagger\bar{\mathbf{u}}, \end{aligned}$$

where  $\bar{Z} = \bar{U}\bar{Y}^\dagger\bar{Y}$ . It can be seen that the encoder is exactly the same as the decoder of **nPOP** approach. Therefore, the inverse test error estimation is

$$(2.9) \quad \epsilon_{\mathbf{u}^{\text{test}}}^{\text{nOP0}} = \epsilon_{\mathbf{u}^{\text{test}}}^{\text{nPOP}} = \left\| \left( \bar{U}\bar{Y}^\dagger G^B - I \right) (\mathbf{u}^{\text{test}} - \bar{\mathbf{u}}) \right\|_2^2.$$

For the decoder, we first rewrite the predicted PtO solution as

$$\begin{aligned} \mathbf{y}^{\text{nOP0}} &= W_d^* \mathbf{u}^{\text{test}} + \mathbf{b}_d^* \mathbf{1}^T = \bar{Y} \left( \bar{Z}^\dagger - \bar{U}^\dagger + \bar{U}^\dagger \right) \mathbf{u}^{\text{test}} + \bar{\mathbf{y}} - \bar{Y} \left( \bar{Z}^\dagger - \bar{U}^\dagger + \bar{U}^\dagger \right) \bar{\mathbf{u}} \\ &= G \mathbf{u}^{\text{test}} + \bar{Y} \left( \bar{Z}^\dagger - \bar{U}^\dagger \right) (\mathbf{u}^{\text{test}} - \bar{\mathbf{u}}). \end{aligned}$$

It implies the the PtO map prediction error can be expressed as

$$\epsilon_{\mathbf{y}^{\text{test}}}^{\text{nOP0}} = \left\| \mathbf{y}^{\text{nOP0}} - \mathbf{y}^{\text{test}} \right\|_2^2 = \left\| \bar{Y} \left( \bar{Z}^\dagger - \bar{U}^\dagger \right) (\mathbf{u}^{\text{test}} - \bar{\mathbf{u}}) \right\|_2^2.$$

It can be seen that the decoder is not able to learn the PtO map  $G^B$  exactly even if a large amount of training data is available. Indeed, there is always a deviation due to error induced by the mismatch in inverted solutions obtained by the encoder solutions  $\bar{Z}$  and ground truth training data  $\bar{U}$ . Note that this error is inevitable since the encoder is not able to reconstruct the true  $U$  due to the ill-posed nature of the inverse map.

**2.3. Model constrained autoencoder learning approaches.** In this section, we present two model-constrained AutoEncoder approaches that incorporate the forward model  $\mathcal{G}$  into the loss function. As we shall show, *introducing the physics/discretization via the forward map provides better inverse surrogate models than naïve AutoEncoder approaches, presented in [subsection 2.2](#). The model-constrained AutoEncoder approaches can also learn the PtO/forward maps with only one training data sample.*

**2.3.1. Model-constrained autoEncoder PtO-inverse learning approach mcPOP.** We propose a model-constrained AutoEncoder learning approach, **mcPOP**, in which the encoder learns the PtO map and the decoder learns the inverse map. As opposed to **nPOP**, **mcPOP** adds a model-constrained term that takes the predicted inverse solution from the decoder and reproduces the observation via the PtO map,  $G^B$ . The loss functions for **mcPOP** are expressed as

$$(2.10) \quad \begin{aligned} \Psi_e^* &= \min_{\Psi_e} \frac{1}{2} \|\Psi_e(U) - Y\|_F^2, \\ \Psi_d^* &= \min_{\Psi_d} \frac{1}{2} \|\Psi_d(\Psi_e^*(U)) - U\|_F^2 + \frac{\lambda}{2} \|B \circ \mathcal{G}(\Psi_d(\Psi_e^*(U))) - Y\|_F^2. \end{aligned}$$

Following the same procedure for linear problems using a linear neural network, the loss functions for **mcPOP** reads



$$(2.10) \quad \begin{aligned} W_e^*, \mathbf{b}_e^* &= \min_{W_e, \mathbf{b}_e} \frac{1}{2} \|W_e U + \mathbf{b}_e \mathbf{1}^T - Y\|_F^2, \\ W_d^*, \mathbf{b}_d^* &= \min_{W_d, \mathbf{b}_d} \frac{1}{2} \|W_d Z + \mathbf{b}_d \mathbf{1}^T - U\|_F^2 + \frac{\lambda}{2} \|G^B (W_d Z + \mathbf{b}_d \mathbf{1}^T) - Y\|_F^2, \end{aligned}$$

where  $Z = W_e^* U + \mathbf{b}_e^* \mathbf{1}^T$ . By apply the first optimality condition, the optimal solutions for (2.10) for linear problems (derived in subsection 5.3) are

$$(2.11) \quad \begin{aligned} W_e^* &= G^B \bar{U} \bar{U}^\dagger, & \mathbf{b}_e^* &= G^B (I - \bar{U} \bar{U}^\dagger) \bar{\mathbf{u}}, \\ W_d^* &= (I + \lambda G^{B^T} G^B)^{-1} (\bar{U} \bar{Y}^\dagger + \lambda G^{B^T} \bar{Y} \bar{Y}^\dagger), \\ \mathbf{b}_d^* &= (I + \lambda G^{B^T} G^B)^{-1} (\bar{\mathbf{u}} + \lambda G^{B^T} \bar{\mathbf{y}} - (\bar{U} \bar{Y}^\dagger + \lambda G^{B^T} \bar{Y} \bar{Y}^\dagger) \bar{\mathbf{y}}). \end{aligned}$$

It can be seen that the encoder is identical to the encoder obtained from **nPOP**. If a sufficient amount of data is available, i.e.,  $\bar{U}$  is full row rank, the PtO map  $G^B$  can be learned well by the encoder, and thus  $\boldsymbol{\varepsilon}_{\mathbf{y}^{\text{test}}}^{\text{mcPOP}} = 0$ . On the other hand, the inverse solutions obtained by the decoder turn out the same as the solution of the Tikonov regularization approach. Specifically, given an observation sample  $\mathbf{y}^{\text{test}}$ , the inverse solution  $\mathbf{u}^{\text{mcPOP}}$  can be derived as

$$\mathbf{u}^{\text{mcPOP}} = (I + \lambda G^{B^T} G^B)^{-1} (\bar{\mathbf{u}} + \lambda G^{B^T} \bar{\mathbf{y}} + (\bar{U} \bar{Y}^\dagger + \lambda G^{B^T} \bar{Y} \bar{Y}^\dagger) (\mathbf{y}^{\text{test}} - \bar{\mathbf{y}}))$$

which is exactly the solution of the following Tikonov regularization problem

$$\min_{\mathbf{u}} \frac{1}{2} \|\mathbf{u} - \mathbf{u}^{\text{mc}}\|_2^2 + \frac{\lambda}{2} \|G^B \mathbf{u} - \mathbf{y}^{\text{test}}\|_2^2,$$

where

$$\mathbf{u}^{\text{mc}} = \bar{\mathbf{u}} + \bar{U} \bar{Y}^\dagger (\mathbf{y}^{\text{test}} - \bar{\mathbf{y}}) - \lambda G^{B^T} (I - \bar{Y} \bar{Y}^\dagger) (\mathbf{y}^{\text{test}} - \bar{\mathbf{y}}).$$

The corresponding error of predicted inverse solution  $\mathbf{u}^{\text{mcPOP}}$  can be derived as

$$(2.12) \quad \begin{aligned} \boldsymbol{\varepsilon}_{\mathbf{u}^{\text{test}}}^{\text{mcPOP}} &= \|\mathbf{u}^{\text{mcPOP}} - \mathbf{u}^{\text{test}}\|_2^2 \\ &= \left\| \left( I + \lambda G^{B^T} G^B \right)^{-1} \left( (\bar{U} \bar{Y}^\dagger G^B - I) (\mathbf{u}^{\text{test}} - \bar{\mathbf{u}}) + \lambda G^{B^T} (I - \bar{Y} \bar{Y}^\dagger) G^B (\mathbf{u}^{\text{test}} - \bar{\mathbf{u}}) \right) \right\|_2^2. \end{aligned}$$

It can be seen that if a sufficient amount of training data is given such that  $\bar{Y} \bar{Y}^\dagger = I$ , the error of predicted inverse solution  $\mathbf{u}^{\text{mcPOP}}$  is lower by a factor of  $(I + \lambda G^{B^T} G^B)^{-1}$  compared to **nPOP** and **nOPO**. This observation reveals the key benefit of the model-constrained AutoEncoder approach in learning the inverse map compared to the pure data-driven counterparts. However, we emphasize that the error of predicted inverse solution  $\mathbf{u}^{\text{mcPOP}}$  is still data-dependent in that the inverse error is proportional to the distance  $(\mathbf{u}^{\text{test}} - \bar{\mathbf{u}})$ . In other words, it could have strongly bias to the mean of training data  $\bar{\mathbf{u}}$ . This bias could lead to poor generalization of the inverse surrogate model.

**2.3.2. Model-constrained autoencoder inverse-PtO learning approach mcPOP.** Conversely, we consider a model-constrained AutoEncoder inverse-PtO learning approach, **mcOPO**, in which the encoder learns the inverse map and the decoder learn the PtO map. Unlike **nOPO**, the encoder output is fed to the PtO model to reproduce observation data. As shown in **mcPOP** approach, this model-constrained strategy provides a better inverse solution surrogate model. Additionally, we learn the decoder by minimizing the misfit between decoder outputs and PtO maps, whose inputs are any outputs from encoder networks during training. The loss functions for **mcOPO** approach read

$$(mcOPO) \quad \begin{aligned} \Psi_e^* &= \min_{\Psi_e} \frac{1}{2} \|\Psi_e(Y) - U\|_F^2 + \frac{\lambda}{2} \|B \circ \mathcal{G}(\Psi_e(Y)) - Y\|_F^2, \\ \Psi_d^* &= \min_{\Psi_d} \frac{1}{2} \|\Psi_d(\Psi_e^*(Y)) - B \circ \mathcal{G}(\Psi_e^*(Y))\|_F^2. \end{aligned}$$

Similarly to previous analysis for other approaches, we apply to the linear problems with linear encoder and decoder neural networks, the loss functions for **mcOPO** are given as

$$(2.13) \quad \begin{aligned} W_e^*, \mathbf{b}_e^* &= \min_{W_e, \mathbf{b}_e} \frac{1}{2} \|W_e Y + \mathbf{b}_e \mathbf{1}^T - U\|_F^2 + \frac{\lambda}{2} \|G^B(W_e Y + \mathbf{b}_e \mathbf{1}^T) - Y\|_F^2, \\ W_d^*, \mathbf{b}_d^* &= \min_{W_d, \mathbf{b}_d} \frac{1}{2} \|W_d(W_e^* Y + \mathbf{b}_e^* \mathbf{1}^T) + \mathbf{b}_d \mathbf{1}^T - G^B(W_e^* Y + \mathbf{b}_e^* \mathbf{1}^T)\|_F^2. \end{aligned}$$

By applying the first optimality condition, the optimal solutions for (2.13) as derived in subsection 5.4 are

$$(2.14) \quad \begin{aligned} W_e^* &= (I + \lambda G^{B^T} G^B)^{-1} (\bar{U} \bar{Y}^\dagger + \lambda G^{B^T} \bar{Y} \bar{Y}^\dagger), \\ \mathbf{b}_e^* &= (I + \lambda G^{B^T} G^B)^{-1} (\bar{\mathbf{u}} + \lambda G^{B^T} \bar{\mathbf{y}} - (\bar{U} \bar{Y}^\dagger + \lambda G^{B^T} \bar{Y} \bar{Y}^\dagger) \bar{\mathbf{y}}), \\ W_d^* &= G^B \bar{Z} \bar{Z}^\dagger, \quad \mathbf{b}_d^* = G^B (I - \bar{Z} \bar{Z}^\dagger) \bar{\mathbf{z}}, \end{aligned}$$

where

$$(2.15) \quad \begin{aligned} \bar{\mathbf{z}} &= (I + \lambda G^{B^T} G^B)^{-1} (\bar{\mathbf{u}} + \lambda G^{B^T} \bar{\mathbf{y}}), \\ \bar{Z} &= (I + \lambda G^{B^T} G^B)^{-1} [\bar{U} \bar{Y}^\dagger \bar{Y} + \lambda G^{B^T} \bar{Y}]. \end{aligned}$$

It can be seen that the encoder learns exactly the same inverse map as the decoder in **mcPOP** approach. Therefore, we have  $\epsilon_{\mathbf{u}^{\text{test}}}^{\text{mcOPO}} = \epsilon_{\mathbf{u}^{\text{test}}}^{\text{mcPOP}}$ . On the other hand, for the learned decoder, we can see that as long as  $\bar{Z}$ , or equivalent  $\bar{Y}$ , is full row rank, the PtO map  $G^B$  can be learned well by the decoder. Unlike, the naïve data-driven approaches **nPOP** where we need  $\bar{U}$  is full row rank or **nOPO** where it is impossible to construct the exact inverse map, **mcPOP** can learn exactly the PtO map with only one observation sample, i.e.,

$$(2.16) \quad \Psi_d^*(\mathbf{u}^{\text{test}}) = G^B \mathbf{u}^{\text{test}} = \mathbf{y}^{\text{test}}$$

. Indeed, the condition of full row rank  $Y$  can be satisfied in two ways: a sufficient amount of training data is given, or columns of  $\bar{Y}$  are simply randomized observation samples from a single observation sample [22]. Consequently, we have a zero PtO error estimation,  $\epsilon_{\mathbf{y}_{\text{test}}}^{\text{mcOPO}} = 0$  (at least with high probability).

**Model-constrained autoencoder inverse-forward learning approach mcOPO-Full1.** Observed the advantages of mcOPO approach on learning the PtO map by only one single training sample (2.16), we propose a model-constrained AutoEncoder inverse-forward learning approach, **mcOPO-Full1**, in which the encoder learns the inverse map and the decoder learn the forward map (parameter to full solution of the PDE). The loss functions for **mcOPO-Full1** are

$$\begin{aligned} \Psi_e^* &= \min_{\Psi_e} \frac{1}{2} \|U - \Psi_e(Y)\|_F^2 + \frac{\lambda}{2} \|Y - B \circ \mathcal{G}(\Psi_e(Y))\|_F^2, \\ \Psi_d^* &= \min_{\Psi_d} \frac{1}{2} \|\mathcal{G}(\Psi_e^*(Y)) - \Psi_d(\Psi_e^*(Y))\|_F^2. \end{aligned} \tag{mcOPO-Full1}$$

Following the similar procedure in subsection 2.3.2 for linear problems using linear neural networks, the optimal solutions for **mcOPO-Full1** are

$$\begin{aligned} W_e^* &= (I + \lambda G^{B^T} G^B)^{-1} (\bar{U} \bar{Y}^\dagger + \lambda G^{B^T} \bar{Y} \bar{Y}^\dagger), \\ \mathbf{b}_e^* &= (I + \lambda G^{B^T} G^B)^{-1} (\bar{\mathbf{u}} + \lambda G^{B^T} \bar{\mathbf{y}} - (\bar{U} \bar{Y}^\dagger + \lambda G^{B^T} \bar{Y} \bar{Y}^\dagger) \bar{\mathbf{y}}) \\ W_d^* &= G \bar{Z} \bar{Z}^\dagger, \quad \mathbf{b}_d^* = G (I - \bar{Z} \bar{Z}^\dagger) \bar{\mathbf{z}}, \end{aligned} \tag{2.17}$$

where

$$\begin{aligned} \bar{\mathbf{z}} &= (I + \lambda G^{B^T} G^B)^{-1} (\bar{\mathbf{u}} + \lambda G^{B^T} \bar{\mathbf{y}}), \\ \bar{Z} &= (I + \lambda G^{B^T} G^B)^{-1} [\bar{U} \bar{Y}^\dagger \bar{Y} + \lambda G^{B^T} \bar{Y}]. \end{aligned} \tag{2.18}$$

It can be seen that the encoder is identical to the one obtained by mcPOP, mcOPO, thus the inverse error estimate is  $\epsilon_{\mathbf{u}_{\text{test}}}^{\text{mcOPO-Full1}} = \epsilon_{\mathbf{u}_{\text{test}}}^{\text{mcOPO}} = \epsilon_{\mathbf{u}_{\text{test}}}^{\text{mcPOP}}$ . Meanwhile, the decoder is able to learn the PDEs linear solver  $G$  by only one single observation sample in a similar way that mcOPO approach does, i.e.,  $\epsilon_{\omega_{\text{test}}}^{\text{mcOPO-Full1}} = 0$ .

#### 2.4. TAE: model-constrained Tikhonov autoencoder approaches.

As discussed in the naive and model-constrained approaches, nPOP, nOPO, mcPOP, mcOPO, and mcOPO-Full1, the performance of learned inverse surrogate models depends on the training data samples. In our previous work [56], we proposed TNet, model-constrained Tikhonov neural network, which can learn the inverse map with much fewer training samples than naive and model-constrained approaches. Furthermore, shown above for mcOPO and mcOPO-Full1 with linear models, we can learn the exact PtO and forward map with only one training observation sample.

We now propose a TAE approach which, as will be shown, is able to learn the inverse and PtO map with only one training sample. Further, we emphasize that TAE requires only the

“label” part, namely  $\mathbf{y}$ , of the training samples and the prior mean of the PoI,  $\mathbf{u}_0$ , while no ground truth PoI is needed.<sup>2</sup> The schematic of **TAE** is presented in [Figure 1](#). A sequential learning strategy is applied to learn the encoder and decoder in two phases. In **Phase 1**, at every epoch during training, we randomize the observational data with noise  $\varepsilon \sim \mathcal{N}\left(0, \varepsilon^2 [\text{diag}(\mathbf{y})]^2\right)$  which is added to the observation data  $\mathbf{y}$  to generate randomized observation samples. The randomized data is then fed into the encoder network  $\Psi_e$  to predict the inverse solution  $\mathbf{u}^*$ . The predicted inverse  $\mathbf{u}^*$  is passed to the PtO map  $B \circ \mathcal{G}$  to predict the observation data  $B\omega^*$ . We minimize the encoder loss  $\mathcal{L}_e$  for the encoder network. In **Phase 2**, we randomize observations and pass through the already-trained encoder network to produce inverse solutions  $\mathbf{u}^*$ . Then,  $\mathbf{u}^*$  is treated as inputs to both the decoder network  $\Psi_d$  to produce  $\mathbf{y}^*$  and PtO map to produce  $B\omega^*$ . The decoder loss  $\mathcal{L}_d$  is then minimized to find optimal decoder parameters. In other words, in **Phase 2**, we can consider the encoder as the generative engine that generates physics samples  $\mathbf{u}^*$  to train the PtO surrogate model. The loss functions for **TAE** from [Figure 1](#) are given as

$$(TAE) \quad \begin{aligned} \Psi_e^* &= \min_{\Psi_e} \frac{1}{2} \|\Psi_e(Y) - \mathbf{u}_0 \mathbf{1}^T\|_F^2 + \frac{\lambda}{2} \|B \circ \mathcal{G}(\Psi_e(Y)) - Y\|_F^2, \\ \Psi_d^* &= \min_{\Psi_d} \frac{1}{2} \|\Psi_d(\Psi_e^*(Y)) - B \circ \mathcal{G}(\Psi_e^*(Y))\|_F^2. \end{aligned}$$

For linear problems and linear networks (see previous sections), the loss functions for **TAE** becomes

$$(2.19) \quad \begin{aligned} W_e^*, \mathbf{b}_e^* &= \min_{W_e, \mathbf{b}_e} \frac{1}{2} \|W_e Y + \mathbf{b}_e \mathbf{1}^T - \mathbf{u}_0 \mathbf{1}^T\|_F^2 + \frac{\lambda}{2} \|G^B(W_e Y + \mathbf{b}_e \mathbf{1}^T) - Y\|_F^2, \\ W_d^*, \mathbf{b}_d^* &= \min_{W_d, \mathbf{b}_d} \frac{1}{2} \|\Psi_d(W_e^* Y + \mathbf{b}_e^* \mathbf{1}^T) - G^B(W_e^* Y + \mathbf{b}_e^* \mathbf{1}^T)\|_F^2. \end{aligned}$$

The main difference in **TAE** compared to **mcOPO** is now  $U = \mathbf{u}_0 \mathbf{1}^T$ . It is straightforward to achieve the optimal solutions for (2.19) (as derived in [subsection 5.5](#)) are

$$(2.20) \quad \begin{aligned} W_e^* &= (I + \lambda G^{B^T} G^B)^{-1} (\lambda G^{B^T} \bar{Y} \bar{Y}^\dagger), \\ \mathbf{b}_e^* &= (I + \lambda G^{B^T} G^B)^{-1} (\mathbf{u}_0 + \lambda G^{B^T} \bar{\mathbf{y}} - \lambda G^{B^T} \bar{Y} \bar{Y}^\dagger \bar{\mathbf{y}}), \\ W_d^* &= G^B \bar{Z} \bar{Z}^\dagger, \quad \mathbf{b}_d^* = G^B (I - \bar{Z} \bar{Z}^\dagger) \bar{\mathbf{z}}, \end{aligned}$$

where

$$(2.21) \quad \begin{aligned} \bar{\mathbf{z}} &= (I + \lambda G^{B^T} G^B)^{-1} (\mathbf{u}_0 + \lambda G^{B^T} \bar{\mathbf{y}}), \\ \bar{Z} &= (I + \lambda G^{B^T} G^B)^{-1} (\lambda G^{B^T} \bar{Y}). \end{aligned}$$

---

<sup>2</sup>Tikhonov-type of learning method is thus suitable for most practical situations where we do not have training pairs  $(\mathbf{u}, \mathbf{y})$ , but only the label  $\mathbf{y}$  parts.

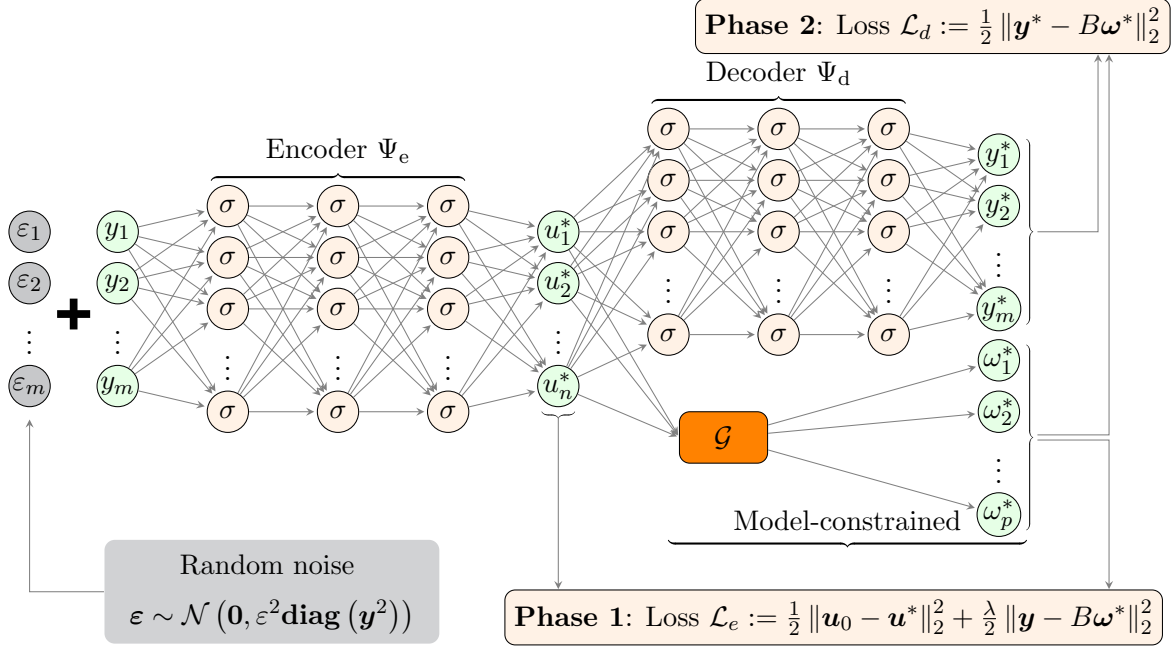


Figure 1: The schematic of **TAE** approach. A sequential learning strategy is applied to learn the encoder and decoder in two phases. In **Phase 1**, at every epoch during training, we randomize the observation data with noise  $\varepsilon \sim \mathcal{N}\left(0, \varepsilon^2 [\mathbf{diag}(\mathbf{y})]^2\right)$  which is added to the observation data  $\mathbf{y}$  to generate randomized observation samples. The randomized data is then fed into the encoder network  $\Psi_e$  to predict the inverse solution  $\mathbf{u}^*$ . The predicted inverse  $\mathbf{u}^*$  is passed to the PtO map  $B \circ \mathcal{G}$  to predict the observation data  $B\omega^*$ . We minimize the encoder loss  $\mathcal{L}_e$  for the optimal encoder network. In **Phase 2**, we randomize observations and pass through the pre-trained encoder network to produce inverse solutions  $\mathbf{u}^*$ . Then,  $\mathbf{u}^*$  is treated as inputs to both the decoder network  $\Psi_d$  to produce  $\mathbf{y}^*$  and PtO map to produce  $B\omega^*$ . The decoder loss  $\mathcal{L}_d$  is then minimized to find optimal decoder parameters.

It can be seen that the **TAE** inverse solution obtained by the encoder network for an observation test sample,  $\mathbf{y}^{\text{test}}$ , is

$$\mathbf{u}^{\text{TAE}} = \left(I + \lambda G^{B^T} G^B\right)^{-1} \left(\mathbf{u}_0 + \lambda G^{B^T} \bar{\mathbf{y}} + \lambda G^{B^T} \bar{\mathbf{Y}} \bar{\mathbf{Y}}^\dagger (\mathbf{y}^{\text{test}} - \bar{\mathbf{y}})\right)$$

which is exactly the inverse solution of the following linear Tikhonov regularization problem

$$\min_{\mathbf{u}} \frac{1}{2} \|\mathbf{u} - \mathbf{u}_0\|_2^2 + \frac{\lambda}{2} \|G^B \mathbf{u} - \mathbf{y}^{\text{test}}\|_2^2.$$

Therefore, the error of inverse solutions obtained from the **TAE** encoder network is

$$(2.22) \quad \begin{aligned} \varepsilon_{\mathbf{u}^{\text{test}}}^{\text{TAE}} &= \|\mathbf{u}^{\text{TAE}} - \mathbf{u}^{\text{test}}\|_2^2 \\ &= \left\| \left( I + \lambda G^{BT} G^B \right)^{-1} \left( \mathbf{u}_0 - \mathbf{u}^{\text{test}} \right) + \lambda G^{BT} \left( I - \bar{Y} \bar{Y}^\dagger \right) \left( \mathbf{y}^{\text{test}} - \bar{\mathbf{y}} \right) \right\|_2^2. \end{aligned}$$

It can be seen that as long as  $\bar{Y}$  is full row rank, which can be obtained with high probability by having large number of randomization observation samples [22], the error can be written as (again with high probability)

$$(2.23) \quad \varepsilon_{\mathbf{u}^{\text{test}}}^{\text{TAE}} = \left\| \left( I + \lambda G^{BT} G^B \right)^{-1} \left( \mathbf{u}_0 - \mathbf{u}^{\text{test}} \right) \right\|_2^2 \leq \|\mathbf{u}_0 - \mathbf{u}^{\text{test}}\|_2^2,$$

independent of the single training sample. On the other hand, similar to the decoder of **mcOPO**, it can be shown that the **TAE** decoder network is able to learn the PtO map exactly,  $\varepsilon_{\mathbf{y}^{\text{test}}}^{\text{TAE}} = 0$ , with only one observation training sample.

**A modified model-constrained autoencoder TAE.** Inspired by advantages of **TAE** and **mcOPO-Full**, we propose a new approach, **TAE-Full**, where the encoder learns the inverse Tikhonov regularization solver and the decoder learns the forward map (parameter to solution of PDEs). We construct the loss for **TAE-Full** as

$$(2.24) \quad \begin{aligned} \Psi_e^* &= \min_{\Psi_e} \frac{1}{2} \|\Psi_e(Y) - \mathbf{u}_0 \mathbf{1}^T\|_F^2 + \frac{\lambda}{2} \|B \circ \mathcal{G}(\Psi_e(Y)) - Y\|_F^2, \\ \Psi_d^* &= \min_{\Psi_d} \frac{1}{2} \|\Psi_d(\Psi_e(Y)) - \mathcal{G}(\Psi_e(Y))\|_F^2. \end{aligned}$$

Analogous to other approaches, in the context of linear problems using linear autoencoder networks, the optimal solutions for encoder and decoder networks are

$$(2.24) \quad \begin{aligned} W_e^* &= (I + \lambda G^{BT} G^B)^{-1} \left( \lambda G^{BT} \bar{Y} \bar{Y}^\dagger \right), \\ \mathbf{b}_e^* &= (I + \lambda G^{BT} G^B)^{-1} \left( \mathbf{u}_0 + \lambda G^{BT} \bar{\mathbf{y}} - \lambda G^{BT} \bar{Y} \bar{Y}^\dagger \bar{\mathbf{y}} \right), \\ W_d^* &= G \bar{Z} \bar{Z}^\dagger, \quad \mathbf{b}_d^* = G \left( I - \bar{Z} \bar{Z}^\dagger \right) \bar{\mathbf{z}}, \end{aligned}$$

where

$$(2.25) \quad \begin{aligned} \bar{\mathbf{z}} &= (I + \lambda G^{BT} G^B)^{-1} \left( \mathbf{u}_0 + \lambda G^{BT} \bar{\mathbf{y}} \right), \\ \bar{Z} &= (I + \lambda G^{BT} G^B)^{-1} \left( \lambda G^{BT} \bar{Y} \right). \end{aligned}$$

It can be seen that the encoder network of **TAE-Full** is exactly the same as encoder network of **TAE**, and thus  $\varepsilon_{\mathbf{u}^{\text{test}}}^{\text{TAE-Full}} = \varepsilon_{\mathbf{u}^{\text{test}}}^{\text{TAE}}$ . Similar to the decoder of **mcOPO-Full**, the decoder network of **TAE-Full** is able to learn the forward map exactly with only one observation training sample, i.e.,  $\varepsilon_{\mathbf{y}^{\text{test}}}^{\text{TAE-Full}} = 0$ .

For clarity, we summarize the error estimations of the proposed approaches in [Table 1](#) and whether or not an approach can learn the PtO/forward and inverse map with only one training sample.

Table 1: Summary of test error estimations obtained from various approaches for solving linear problems using linear encoder and decoder networks.

Approaches	PtO/forward error $\varepsilon_{\mathbf{y}^{\text{test}}} / \varepsilon_{\omega^{\text{test}}}$	Inverse error $\varepsilon_{\mathbf{u}^{\text{test}}}$	Ability to learn with 1 sample
<b>nPOP</b>	0	$\ (\bar{U}\bar{Y}^\dagger G^B - I)(\mathbf{u}^{\text{test}} - \bar{\mathbf{u}})\ _2^2$	None
<b>nOPO</b>	inevitably $> 0$		None
<b>mcPOP</b>	0	$\leq \ (\bar{U}\bar{Y}^\dagger G^B - I)(\mathbf{u}^{\text{test}} - \bar{\mathbf{u}})\ _2^2$	Only PtO
<b>mcOPO(-Full)</b>	0		Only PtO/forward
<b>TAE(-Full)</b>	0	$\leq \ \mathbf{u}^{\text{test}} - \mathbf{u}_0\ _2^2$	All

**2.5. Simultaneous training strategy for encoder and decoder networks.** In this section, we consider the case where the encoder and decoder are trained simultaneously for **nPOP** using the same training data set  $(U, Y)$ . In this scenario, we introduce an extra hyperparameter  $\beta$  to balance the encoder and decoder loss, the loss function reads

$$(2.26) \quad \Psi_e^*, \Psi_d^* = \min_{\Psi_e, \Psi_d} \frac{1}{2} \|\Psi_e(U) - Y\|_F^2 + \frac{\beta}{2} \|\Psi_d(\Psi_e(U)) - U\|_F^2,$$

To gain insights into how different the simultaneous training strategy is compared to the sequential training counterpart, we analyze the same linear problems using linear encoder and decoder networks. By deriving the first optimality condition, we can obtain the optimal weight and bias for the encoder and decoder networks as follows (see [subsection 5.6](#) for full derivation):

$$(2.27) \quad \begin{aligned} W_e^* &= \left(I + \beta W_d^{*T} W_d^*\right)^{-1} \left(G^B \bar{U} \bar{U}^\dagger + \beta W_d^{*T} \bar{U} \bar{U}^\dagger\right), & \mathbf{b}_e^* &= \bar{\mathbf{y}} - W_e^* \bar{\mathbf{u}}, \\ W_d^* &= \bar{U} (W_e^* \bar{U})^\dagger, & \mathbf{b}_d^* &= \bar{\mathbf{u}} - W_d^* \bar{\mathbf{y}}, \\ W_e^* \bar{U} \bar{U}^T &= W_e^* W_d^* W_e^* \bar{U} \bar{U}^T \end{aligned}$$

It can be seen that it is not clear how to derive a closed form solution for the optimal  $W_e^*$ ,  $\mathbf{b}_e^*$ ,  $W_d^*$ ,  $\mathbf{b}_d^*$  since  $W_e^*$  is a nonlinear function of  $W_d^*$ . In other words, even with linear problems, we might need to use some iterative algorithm to obtain a solution. Furthermore, even with sufficient training data, such that  $\bar{U} \bar{U}^\dagger = I$ , the encoder network becomes

$$(2.28) \quad W_e^* = \left(I + \beta W_d^{*T} W_d^*\right)^{-1} \left(G^B + \beta W_d^{*T}\right), \quad \mathbf{b}_e^* = \bar{\mathbf{y}} - W_e^* \bar{\mathbf{u}}.$$

In this case, it is still uncertain how to train the optimal encoder to recover the exact linear PtO map  $G^B$ . As a result, the decoder accuracy will be affected by the outputs from the inaccuracy of the encoder network. Another drawback of the simultaneous training strategy is that tuning the hyperparameter  $\beta$  for the encoder loss and decoder loss is required and problem-dependent, in addition to having a larger training problem to solve. In a special case

of  $\beta = 1$ , one of the sets of optimal solutions  $W_e^*$ ,  $\mathbf{b}_e^*$ ,  $W_d^*$ ,  $\mathbf{b}_d^*$  for (2.26) is indeed identical to the one obtained by the sequential training strategy in (2.4),

$$(2.29) \quad W_e^* = G^B \bar{U} \bar{U}^\dagger, \quad \mathbf{b}_e^* = G^B \left( I - \bar{U} \bar{U}^\dagger \right) \bar{\mathbf{u}}, \quad W_d^* = \bar{U} \bar{Y}^\dagger, \quad \mathbf{b}_d^* = \bar{\mathbf{u}} - \bar{U} \bar{Y}^\dagger \bar{\mathbf{y}}.$$

It can be seen that, with the sequential training strategy,  $W_e^* = G^B$  recovers the exact PtO map if sufficient training  $\bar{U}$  is provided. By contrast, with the simultaneous training strategy in the identical setting, the encoder is not guaranteed to recover the exact PtO map.

**3. Numerical results.** We begin by outlining the training and testing configurations for our proposed approaches for solving forward and inverse problems, focusing on two case studies: the heat equation subsection 3.1 and the Navier-Stokes equation subsection 3.2. Table 2 summarizes the specifications for neural network architectures, training settings, data sets, etc.

Table 2: Summary of training parameters for learning forward and inverse problems in subsection 3.1 and subsection 3.2.

Network	Architecture	1 layer with 5000 neurons
	Activation function	ReLU
	Weight initializer	$\mathcal{N}(0, 0.02)$
	Bias initializer	$\mathbf{0}$
	Random seed	100
Training	Optimizer	ADAM
	Learning rate	$10^{-3}$
	Batch size	$n_t = 100$
Data	Train data	100 samples (drawn independently)
	Test data	500 samples (drawn independently)
	Train random seed	18
	Test random seed	28
Precision	Double precision	

**Data generation.** Our training dataset comprises 100 paired samples of PoIs and their corresponding clean observations  $\mathbf{y}^{\text{clean}}$ , which are subsequently corrupted to  $\mathbf{y}^{\text{test}}$  according to (3.1). We consider two training cases: Case I - single-sample training; and Case II - 100-sample training. In case I, we replicate the randomly chosen sample to create a set of 100 identical samples. In case II, we use all different 100 training samples. For evaluation purposes, we utilize a test dataset of 500 sample pairs, corrupted with noise level  $\delta$  as (3.1), to benchmark different approaches. The Tikhonov inverse solutions are computed using the standard BFGS optimization algorithm [57] available in Jax-Optax [9].



**Two stages of adding noise.** For each sample regardless of case (1) or case (2), we corrupt noise at two stages in our experimental framework. Initially, we introduce a noise level  $\delta$  to the clean synthetic data to simulate real-world scenarios:

$$(3.1) \quad \mathbf{y}^{\text{test}} = \mathbf{y}^{\text{clean}} + \delta \odot \mathbf{y}^{\text{clean}}, \quad \delta \sim \mathcal{N}(0, \delta^2 \mathbf{I}),$$

where  $\odot$  represents element-wise multiplication,  $\mathbf{y}^{\text{clean}}$  denotes the noise-free data generated by the forward solver, and  $\mathbf{I} \in \mathbb{R}^{m \times m}$  is an identity matrix. Subsequently, we perform the data randomization technique. Specifically, per epoch during training, for the **mcOPO**, **mcOPO-Full**, **TAE** and **TAE-Full** methods, we apply an additional noise level  $\varepsilon$  on-the-fly to the already corrupted data  $\mathbf{y}^{\text{test}}$ :

$$(3.2) \quad \tilde{\mathbf{y}}^{\text{rand}} = \mathbf{y}^{\text{test}} + \varepsilon, \quad \varepsilon \sim \mathcal{N}(0, \varepsilon^2 \mathbf{diag}((\mathbf{y}^{\text{test}})^2)).$$

In practice, we generate a randomized sample as follows, drawing standard Gaussian random samples  $\zeta$  and then point-wise multiplication with  $\mathbf{y}^{\text{test}}$  to generate noise realizations, i.e.,

$$\tilde{\mathbf{y}}^{\text{rand}} = \mathbf{y}^{\text{test}} + \zeta \odot \mathbf{y}^{\text{test}}, \quad \zeta \sim \mathcal{N}(0, \varepsilon^2 \mathbf{I}).$$

Specifically, we draw 100 new noise realizations  $\varepsilon$  per epoch and add them to 100 observation samples in both case (1) and case (2). In the meantime, for the **nPOP** and **mcPOP** methods, we retain only the base noise level  $\delta$ , excluding the additional randomization noise level  $\varepsilon$ , as these approaches utilize PoIs as input data. We made this choice considering that introducing excessive noise to PoIs might lead to non-physical or implausible PoI samples leading to unsolvable PDEs. Additionally, for the **nOPO** approach, our experimental results reveal superior performance without the data randomization technique. Thus, we also do not apply  $\varepsilon$  noise level for the **nOPO** approach.

**Accuracy metric.** To evaluate the performance of the learned inverse and PtO/forward mappings across different approaches, we compare the overall accuracy over 500 independent test samples. For the inverse mapping, we employ two error metrics: one based on pointwise absolute error values

$$(3.3) \quad E_{abs,j} = \frac{1}{500} \sum_{i=1}^{500} \left| u_j^{i,\text{pred}} - u_j^{i,\text{true}} \right| \quad j = 1, \dots, n,$$

and another using the relative Euclidean norm error

$$(3.4) \quad E_{rel} = \frac{1}{500} \sum_{i=1}^{500} \frac{\|\mathbf{u}^{i,\text{pred}} - \mathbf{u}^{i,\text{true}}\|_2^2}{\|\mathbf{u}^{i,\text{true}}\|_2^2},$$

where  $i$  indexes the sample number,  $j$  represents the component index of the discretized sample vector, and  $n$  is the number of spatial grid points. The superscripts ‘‘pred’’ and ‘‘true’’ stand for the solution predicted by the neural network and the ground truth parameters of interest, respectively. For the learned PtO mapping, we assess accuracy using the average relative error between predicted observations  $\mathbf{y}^{\text{pred}}$  and true observations  $\mathbf{y}^{\text{true}}$  following (3.4). While

**mcOPO-Full** and **TAE-Full** approaches are developed to learn the forward map predicting the complete solution  $\omega$ , we maintain consistency in comparison by applying the same accuracy metric on  $\mathbf{y} = B\omega$  across all approaches.

**Training settings.** For both heat equation and Navier-Stokes equation, we use a shallow neural network having one hidden layer with 5000 ReLU neurons for both encoder and decoder neural networks. In our previous work [56], we verified that a dense feed-forward neural network architecture with multiple layers, in small data regimes, performs poorly due to the vanishing gradient and/or the bias-variance trade-off issues. We thus focus on neural networks with a single hidden layer and this is sufficient to demonstrate the proposed AutoEncoder frameworks. Regarding the optimization algorithm, the default ADAM [39] optimizer in JAX [9] is used. To ensure fairness across all numerical experiments, we initialize the neural network parameters consistently: weights follow a standard Gaussian distribution while biases are set to zero vectors, all using an identical random seed. This ensures the same initializers across all test cases.

**Sequential training protocol.** Our training strategy follows a sequential two-phase approach. Initially, we optimize the encoder network to maximize accuracy on a test set of 500 samples (for either PoIs or observations, depending on the considering approach). Subsequently, using this pre-trained encoder, we optimize the decoder network to achieve optimal accuracy on the same test dataset size. Our experimental investigations have demonstrated that simultaneous training of both encoder and decoder networks does not yield superior accuracy compared to this sequential approach. This phenomenon can be attributed to two key factors: first, the decoder’s performance is primarily contingent on the quality of the encoder’s output; second, the simultaneous optimization of both networks can compromise encoder accuracy due to the presence of the decoder loss term. The expanded parameter space in simultaneous training increases the likelihood of the optimizer converging to local minima. A theoretical discussion of the simultaneous training strategy compared to the sequential training strategy is presented in subsection 2.5. Therefore, to keep the numerical sections concise, we opt to present the results obtained by sequential training strategy only.

Table 3: **2D heat equation.** Relative error for inverse solutions and forward solutions (observations) obtained by different approaches trained with  $\{1, 100\}$  training samples

Approach	1 training sample		100 training samples	
	Inverse (%)	Forward	Inverse (%)	Forward
nPOP	100.18	$3.99 \times 10^{-1}$	80.48	$5.30 \times 10^{-2}$
nOPO	107.55	$2.90 \times 10^{-1}$	50.18	$1.09 \times 10^{-1}$
mcPOP	107.99	$3.99 \times 10^{-1}$	87.60	$5.30 \times 10^{-2}$
mcOPO	108.28	$2.73 \times 10^{-2}$	46.32	$3.94 \times 10^{-4}$
mcOPO-Full	108.28	$4.21 \times 10^{-2}$	46.32	$4.56 \times 10^{-4}$
TAE	45.23	$1.57 \times 10^{-4}$	45.03	$1.22 \times 10^{-4}$
TAE-Full	45.23	$8.80 \times 10^{-4}$	45.03	$2.12 \times 10^{-4}$
Tik	44.99		44.99	

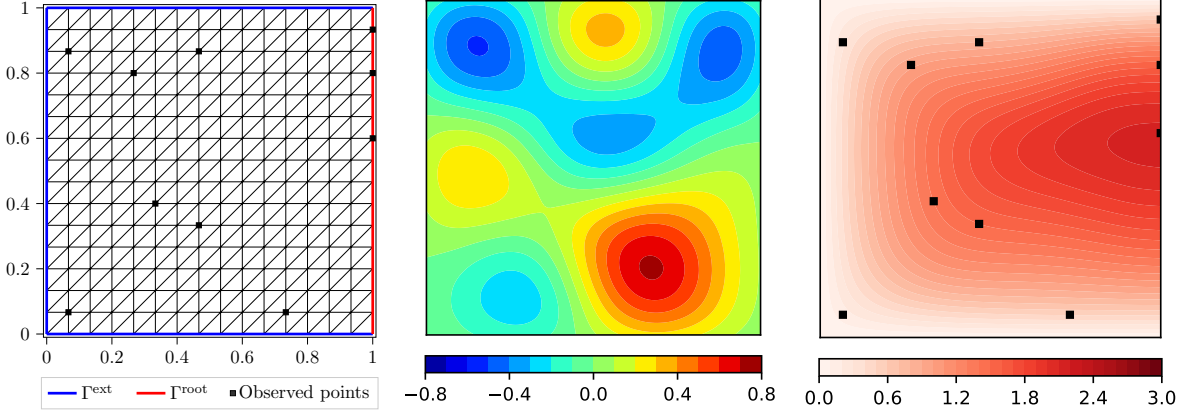


Figure 2: **2D heat equation.** **Left:** Domain, boundary conditions,  $16 \times 16$  finite element discretization mesh, and 10 random observation locations. **Middle:** A sample of the PoI. **Right:** The corresponding state, state observations are taken at 10 observed points. This pair of PoI and observation sample is used for training in one training sample case.

**3.1. 2D heat equation.** We investigate the following heat equation:

$$\begin{aligned} -\nabla \cdot (e^u \nabla \omega) &= 20 & \text{in } \Omega = (0, 1)^2 \\ \omega &= 0 & \text{on } \Gamma^{\text{ext}} \\ \mathbf{n} \cdot (e^u \nabla \omega) &= 0 & \text{on } \Gamma^{\text{root}}, \end{aligned}$$

where  $u$  represents the conductivity coefficient field, which is the parameter of interest - PoI,  $\omega$  denotes the temperature field, and  $\mathbf{n}$  is the unit outward normal vector along the Neumann boundary  $\Gamma^{\text{root}}$ . As illustrated in the left panel of Figure 2, we discretize the domain using a  $16 \times 16$  mesh grid, with 10 randomly distributed observation points sampling from the discretized field  $\omega$ . We aim to achieve two primary goals: (1) learning an inverse mapping to directly reconstruct the conductivity coefficient field  $\mathbf{u}$  from 10 discrete observations  $\mathbf{y} = B\omega$ , and (2) learning a PtO map or forward map that predicts either the temperature observations  $\mathbf{y}$  or the temperature field  $\omega$  given a conductivity coefficient field  $\mathbf{u}$ .

**Generating train and test data sets.** We start with drawing the parameter conductivity samples via a truncated Karhunen-Loéve expansion

$$(3.5) \quad u(x) = \sum_{i=1}^q \sqrt{\lambda_i} \phi_i(x) z_i, \quad x \in [0, 1]^2,$$

where  $(\lambda_i, \phi_i)$  is the eigenpair of a two-point correlation function from [16], and  $\mathbf{z} = (z_i)_{i=1}^n \sim \mathcal{N}(0, I)$  is a standard Gaussian random vector. We choose  $q = 15$  eigenvectors corresponding to the first 15 largest eigenvalues. For each sample, we discretize conductivity coefficient  $u(x)$ , denoted as  $\mathbf{u}$ , and we solve the heat equation for the temperature field  $\omega$  by finite element method. The observation samples  $\mathbf{y}^{\text{clean}}$  are constructed by extracting values of

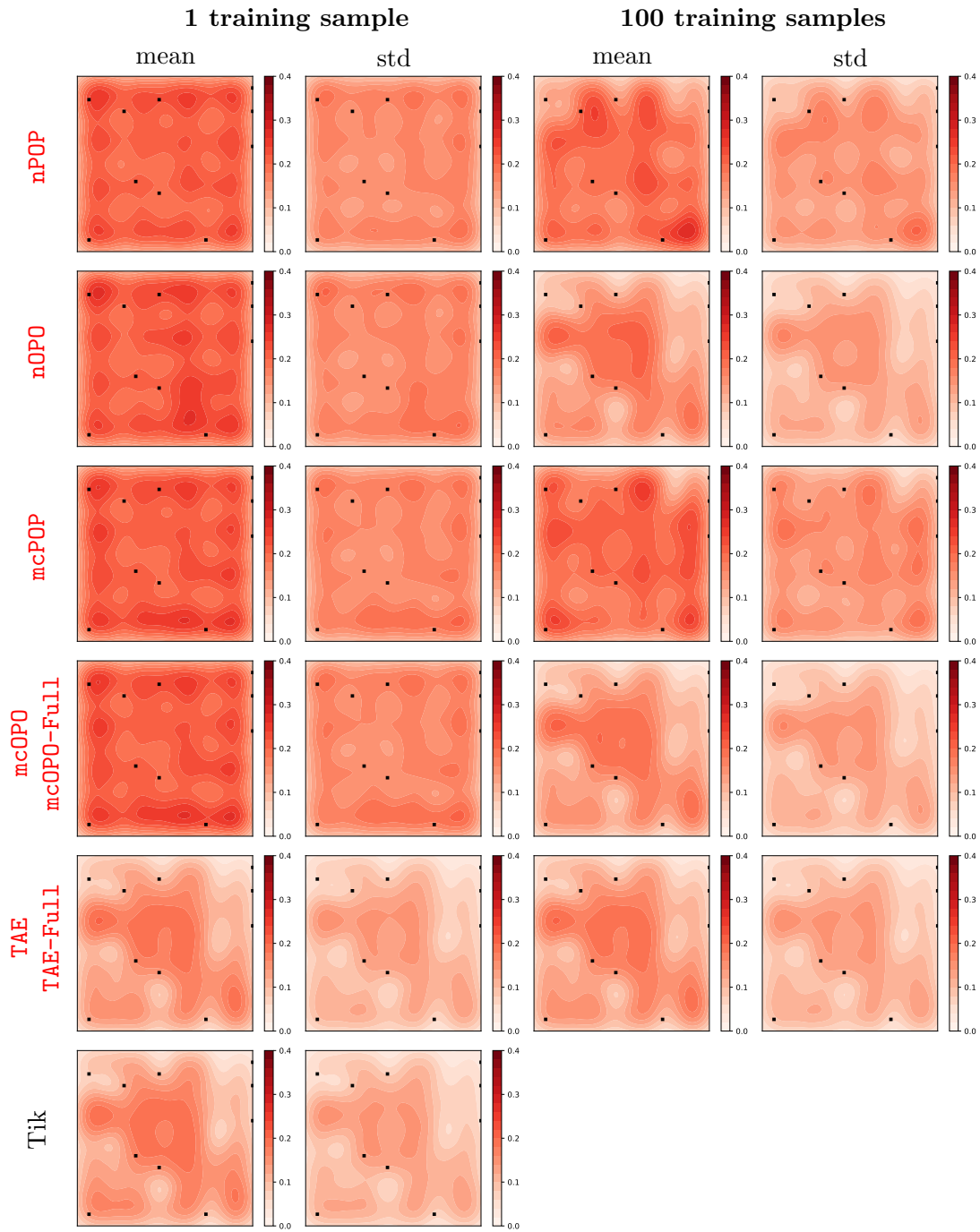


Figure 3: **2D heat equation.** Mean and standard deviation of absolute error of 500 test inverse solutions obtained from different approaches. Black points are observation locations.

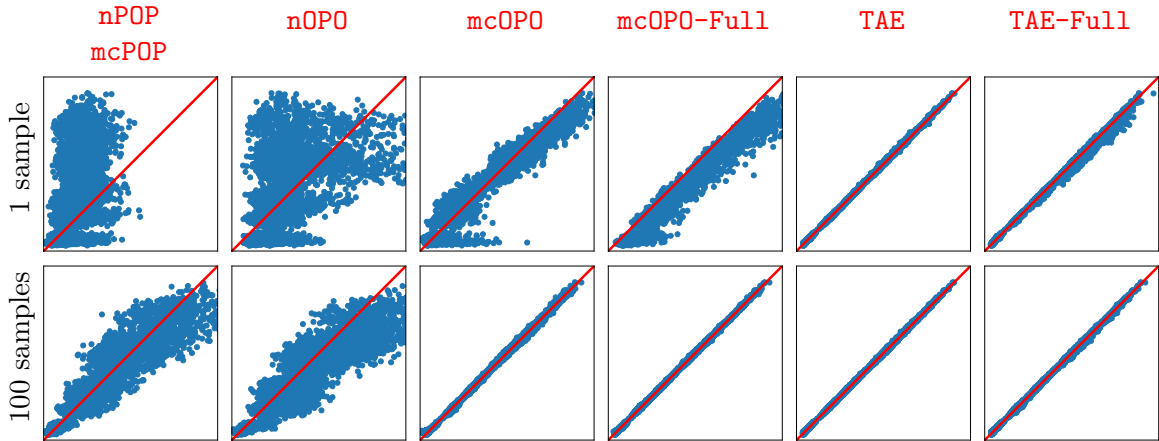


Figure 4: **2D heat equation.** The comparison of 500 test predicted observations obtained from different approaches. The red line indicates the perfect matching between predictions and ground truth observation data set. **Top row:** Trained with 1 training sample. **Bottom row:** Trained with 100 training samples. In all plots plot, the x-axis is the magnitude of the true observation, and the y-axis is the magnitude of the predicted observation, both axes has range of  $[0, 3]$ .

the temperature field  $\omega$  at 10 predetermined random observable locations, followed by the addition of Gaussian noise with the noise level of  $\delta = 0.5\%$ . Our training dataset consists of 100 independently drawn sample pairs. The central and right figures in Figure 2 illustrate the conductivity coefficient field  $\mathbf{u}$  and its corresponding temperature field  $\omega$  for the first pair out of 100 training sample pairs. This particular pair serves as the training data for the single-sample training case across all approaches. For the inference step, we generate 500 independently drawn pairs  $(\mathbf{u}, \omega)$  following the same procedure, and extract for observable  $\mathbf{y}$  as necessitated based on approaches.

**Learned inverse and PtO/forward maps accuracy.** We compare all approaches using a two-phase sequential training protocol: first optimizing the encoder, then training the decoder using the pre-trained encoder. All methods are implemented under two scenarios: training with a single training sample and training with 100 training samples. For the **mcOPO**, **mcOPO-Full**, **TAE** and **TAE-Full** approaches, we carry out per-epoch data randomization during training, adding random noise with magnitude  $\varepsilon = 10\%$  to the corrupted observation samples as specified in (3.2). Table 3 summarizes the relative errors of 500 test samples, calculated according to (3.4), for both inverse and predicted observable solutions across all approaches in both training scenarios.

Analysis of the single-sample training scenario reveals that only the **TAE** and **TAE-Full** approaches achieve robust performance across both forward and inverse solutions. Notably, these approaches attain an inverse solution accuracy of 45.23%, comparable to the traditional Tikhonov regularization method’s 44.99%. In contrast, all other methodologies (**nPOP**, **nOPO**, **mcPOP**, **mcOPO**, and **mcOPO-Full**) fail to produce meaningful results, exhibiting errors exceeding

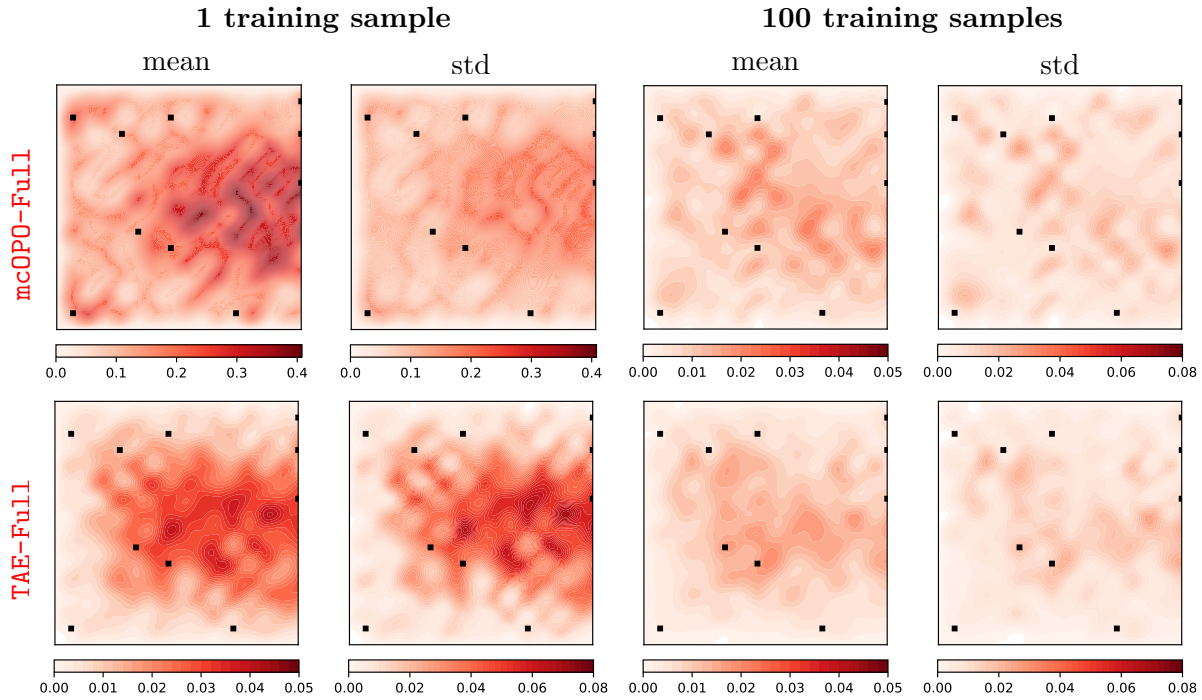


Figure 5: **2D heat equation.** Mean and standard deviation of absolute error of 500 test state solutions obtained from **TAE-Full**. Black points are observation locations.

100%. This performance disparity stems from the superior generalization capability of **TAE** and **TAE-Full** approaches, while other methods suffer from overfitting to the provided training sample. Specifically, as presented in subsection 2.4, **TAE** and **TAE-Full** integrated with data randomization technique allows to learn the inverse map as good as Tikhonov regularization framework for linear inverse problems with only one arbitrary observation training sample. For the weakly nonlinear heat equation inverse problem, the data randomization technique serves two crucial functions: it enables exploration of the unseen test observation sample space while maintaining consistency with the forward solver via model-constrained term. These benefits induced by data randomization allow **TAE** and **TAE-Full** to maintain their great generalization properties as expected in linear problems. Conversely, all other approaches, even including those constrained by forward solvers like **mcPOP**, **mcOPO**, and **mcOPO-Full**, exhibit a strong bias toward the single training sample, as analyzed in subsection 2.2 and subsection 2.3. In terms of learning PtO/forward maps, **TAE** and **TAE-Full** can achieve highly accurate predictions of temperature solutions through the PtO/forward map (decoder), achieving relative errors of  $1.57e-04$  and  $8.80e-04$ , respectively. This demonstrates their capability to learn precise PtO/forward mappings from a single observation sample. Notably, **TAE** achieves superior forward solution accuracy compared to **TAE-Full**, attributed to its direct regularization at observation points rather than minimizing discrepancies across the entire domain discretization points in **TAE-Full** framework. While our analysis in subsection 2.3.2 indicates that

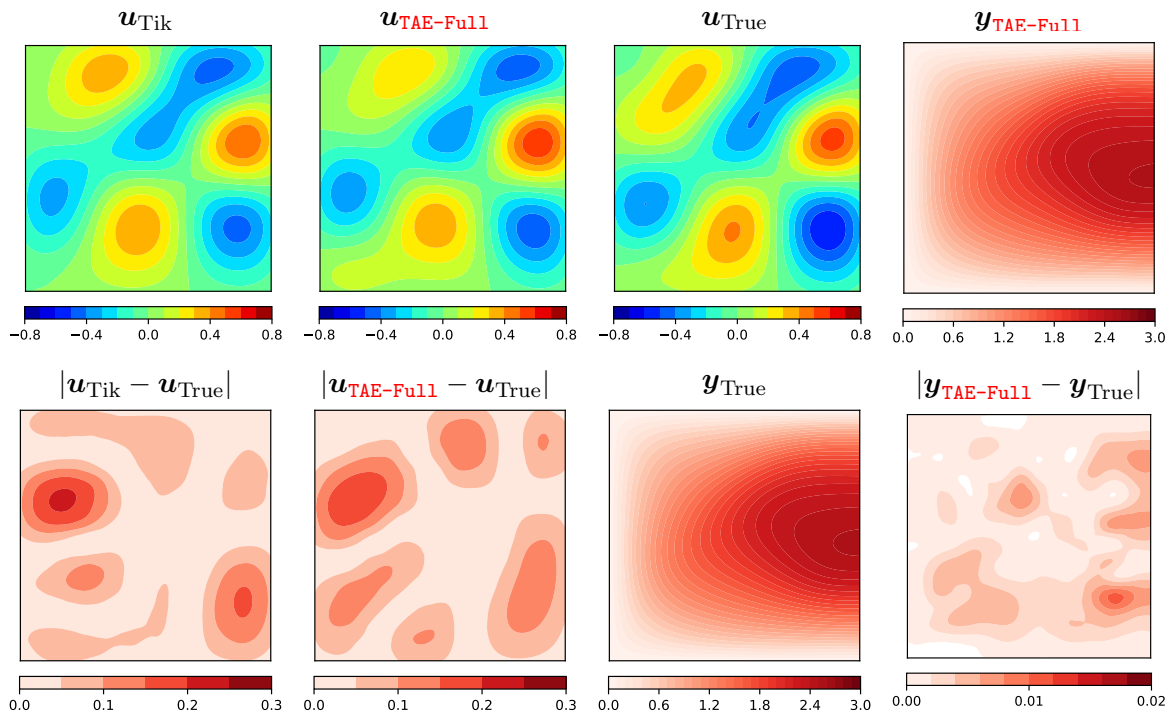


Figure 6: **2D heat equation.** A sample of inverted conductivity coefficient field and temperature field solution obtained by **TAE-Full** trained with 1 training sample coupled with data randomization of noise level  $\sigma = 0.1$ .

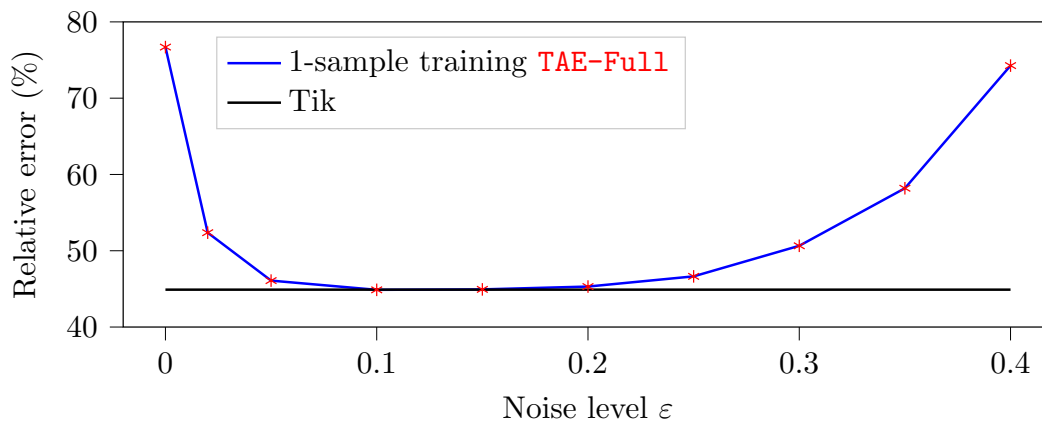


Figure 7: **2D heat equation.** Relative error of inverse solution over 500 test samples with different noise levels.

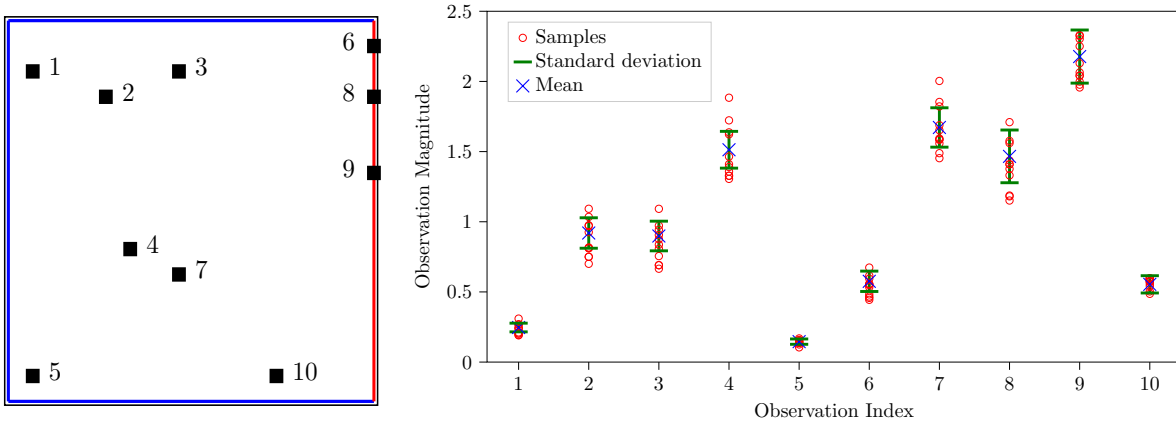


Figure 8: **2D heat equation.** **Left:** Index of 10 observation locations. **Right:** Mean and standard deviation of observation magnitudes of 10000 true observation samples at observation locations. And the observation magnitudes of 10 different observation samples for single-sample training case.

**mcOPO** and **mcOPO-Full** can theoretically learn exact PtO/forward maps in linear problems, their actual performance (errors of  $2.73\text{e-}02$  and  $4.21\text{e-}2$ , respectively) falls short of **TAE** and **TAE-Full**. This underperformance can be attributed to two key factors: inaccurate inverse solutions obtained from the encoder and the weakly nonlinear nature of our heat equation forward problem. On the other hand, the approaches **nPOP**, **nOPO**, and **mcPOP** yield imprecise PtO mappings, which is consistent with their purely data-driven architecture and absence of physical constraints in their formulation.

For the case of training with a sufficiently large data set of 100 samples, the accuracy of forward and inverse maps of all approaches is improved, as expected from the increase in provided training information. **TAE** and **TAE-Full** maintain their superior performance across both PtO/forward and inverse solutions. We emphasize that the best inverse map obtained from **TAE** and **TAE-Full** is just as good as Tikhonov regularization method, thus not much improvement is observed compared to the single-sample training case. The **mcOPO** and **mcOPO-Full** approaches rank second in performance for both inverse and PtO/forward solutions. Unlike the single-sample training scenario, these approaches now achieve reliable inverse maps (encoders), enabling their model-constrained decoders to attain high accuracy in PtO/forward solutions. In the meantime, the purely data-driven **nOPO** approach, lacking physics constraints, yields lower accuracy in inverse solutions compared to **mcOPO**. Furthermore, as analyzed in [subsection 2.2.2](#), the inaccurate inverse solutions from its encoder network inevitably lead to poor PtO solutions, resulting in the lowest overall performance. On the other hand, the **nPOP** and **mcPOP** approaches, which prioritize learning the PtO map (encoder), achieve better PtO solution accuracy than their **nOPO** peer. However, due to the weakly nonlinear nature of our heat equation, the encoder network is not guaranteed to represent exactly the PtO map. Consequently, the imprecise encoder outputs propagate through the decoder, resulting in the least



accurate inverse solutions, even with physics-constrained forward solvers.

We further elaborate the predicted forward and inverse solutions and errors obtained from all approaches. The comparison of mean and standard deviation of pointwise absolute error (3.3) across the physic domain of 500 test inverse solutions obtained from different approaches is presented in Figure 3. It can be seen that the TAE and TAE-Full approaches trained with only one training sample provide the accuracy on inverse solutions as good as the Tikhonov regularization framework, maintaining this performance level with 100 training samples. In contrast, with only one training sample, all other approaches exhibit significantly elevated error mean and error standard deviation relative to Tikhonov regularization approach. Analysis of the 100-sample training scenario reveals that mcOPO and mcOPO-Full frameworks achieve the second-best performance metrics, while nPOP and mcPOP approaches yield the largest deviations from true observations. It is worth noting that there is a significant spatial correlation between the observation locations and lowest error mean and standard deviation in TAE and TAE-Full approaches as well as the classical Tikhonov regularization framework. It further reveals that the TAE and TAE-Full approaches have a great agreement with Tikhonov regularization framework in terms of inverse solutions.

For PtO/forward surrogate models, Figure 4 shows the comparison of 500 predicted test observations obtained from different approaches and ground truth observation. It can be seen that the TAE and TAE-Full approaches demonstrate superior accuracy in PtO solutions as trained with either only one or 100 training samples. Interestingly, TAE-Full provides slightly worse than TAE since the former is regularized with all points over the whole domain while the latter is regularized only at observation points. In contrast, mcOPO and mcOPO-Full approaches are only able to achieve accurate observations as being trained with 100 training samples due to their training data bias nature. In the meantime, nPOP, mcPOP, and nOPO approaches return inaccurate observations even if trained with 100 training samples, consistent with the previously discussed limitations. Among approaches, mcOPO-Full and TAE-Full approaches are able to represent the numerical PDE solvers. The spatial distribution of prediction errors is further examined in Figure 5, which depicts the mean and standard deviation of absolute errors across the domain for 500 test temperature field samples. It can be seen that TAE-Full framework demonstrates consistently lower error statistics compared to mcOPO-Full, with this performance differential particularly pronounced in the single-sample training scenario. These results provide additional validation of the TAE-Full framework's efficacy in learning forward mappings for PDE solutions.

**TAE-Full is the best for learning both inverse and forward surrogate models.**

According to shown numerical results, TAE-Full can be considered as the best framework for learning the inverse and forward surrogate models. Figure 6 shows a test case of inverted conductivity coefficient field and full temperature field solutions obtained by TAE-Full trained with one training sample coupled with data randomization of noise level  $\varepsilon = 10\%$ . It can be seen that the inverted conductivity field exhibits accuracy comparable to the Tikhonov regularization solution, thus closely approximating the true conductivity field distribution. In the meantime, the predicted temperature field demonstrates excellent agreement with the ground truth solution. These results underscore the effectiveness of combining model-constrained learning with data randomization techniques in the TAE-Full framework. Furthermore, the significant dissimilarity between the training sample shown in Figure 2 and the test case

presented in Figure 6 demonstrates the framework’s robust generalization capabilities to completely different test samples. This characteristic enables the development of inverse and forward surrogate models using minimal training data—specifically, a single training sample without ground truth PoI—while maintaining reliable performance on previously unseen test cases.

**TAE-Full robustness to a wide range of noise levels.** We further investigate the robustness of TAE-Full across varying noise levels using a single training sample. Figure 7 demonstrates that TAE-Full achieves relative errors comparable to the Tikhonov regularization framework across a broad noise spectrum (8% to 20%) for 500 test inverse solutions. The framework’s performance exhibits sensitivity to noise levels outside this optimal range, with errors increasing at both extremes. At low noise levels, the data randomization technique insufficiently explores the space of potential unseen test samples, limiting generalization capabilities. Conversely, excessive noise levels result in overwhelmingly corrupted samples becoming statistically indistinguishable, degrading the accuracy of the learned surrogate models. Notably, the minimum relative error achieved by TAE-Full matches that of the Tikhonov regularization framework, indicating that TAE-Full successfully learns to emulate—rather than surpass Tikhonov regularization performance using only a single training sample without requiring ground truth PoI data.

**TAE-Full robustness to arbitrary individual samples for single-sample training case.** In this section, we investigate the robustness of the TAE-Full framework to one arbitrarily chosen sample for training. To that end, ten independent training instances are conducted, each utilizing a single sample randomly selected from a pool of 100 training samples. The left figure in Figure 8 presents the spatial distribution of 10 observation points, including their location indices. Meanwhile, the right figure of Figure 8 shows the statistical characteristics (mean and standard deviation) of 10000 distinct observation samples, and the observation magnitudes for the 10 randomly selected training cases at their respective locations. Statistical analysis of the TAE-Full performance across these 10 distinct training instances yields an average relative error of 45.32% with a standard deviation of 0.32% for inverse solutions. This small variance in relative error metrics demonstrates the TAE-Full approach’s robustness capabilities when trained with an arbitrary individual sample in single-sample training scenarios.

**3.2. Navier-Stokes equations.** The vorticity form of 2D Navier–Stokes equation for viscous and incompressible fluid [47] is written as

$$\begin{aligned} \partial_t \omega(x, t) + v(x, t) \cdot \nabla \omega(x, t) &= \nu \Delta \omega(x, t) + f(x), & x \in (0, 1)^2, t \in (0, T] \\ \nabla \cdot v(x, t) &= 0, & x \in (0, 1)^2, t \in (0, T] \\ \omega(x, 0) &= u(x), & x \in (0, 1)^2 \end{aligned}$$

where  $v \in (0, 1)^2 \times (0, T]$  denotes the velocity field,  $\omega = \nabla \times v$  represents the vorticity, and  $u$  defines the initial vorticity which is the parameter of interest. The forcing function is specified as  $f(x) = 0.1 (\sin(2\pi(x_1 + x_2)) + \cos(2\pi(x_1 + x_2)))$ , with viscosity coefficient  $\nu = 10^{-3}$ . The computational domain is discretized using a uniform  $32 \times 32$  mesh in space, while the temporal domain  $t \in (0, 10]$  is partitioned into 1000 uniform time steps with  $\Delta t = 10^{-2}$ . The

inverse problem aims to reconstruct the initial vorticity field  $\mathbf{u}$  from vorticity measurements  $\mathbf{y}$  collected at 20 random spatial locations at the final time  $T = 10$ .

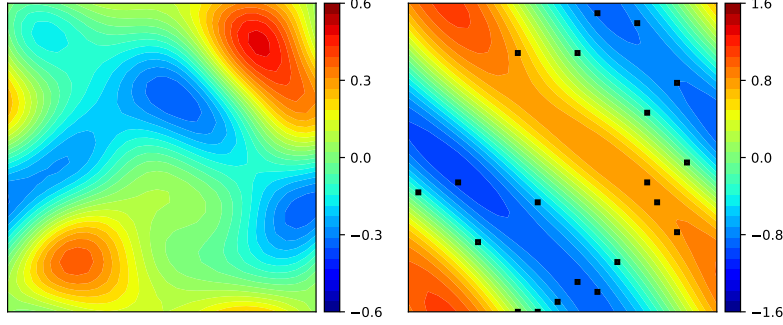


Figure 9: **2D Navier–Stokes equation.** **Left:** A sample of the PoI  $\mathbf{u}$ . **Right:** A corresponding vorticity field  $\omega$  at final time  $T = 10$ , observation  $\mathbf{y}$  are extracted at 20 random observed points. This pair of PoI and observation/vorticity field is used for training in one training sample case.

Table 4: **2D Navier–Stokes equation.** Relative error for inverse solutions and PtO/forward solutions obtained by different approaches trained with  $\{1, 100\}$  training samples

Approach	1 training sample		100 training samples	
	Inverse (%)	Forward	Inverse (%)	Forward
nPOP	156.99	$2.99 \times 10^{-1}$	72.22	$6.72 \times 10^{-2}$
nOPO	103.94	5.60	40.20	$5.94 \times 10^{-1}$
mcPOP	161.48	$2.99 \times 10^{-1}$	76.33	$6.72 \times 10^{-2}$
mcOPO	46.43	$5.15 \times 10^{-1}$	27.29	$2.20 \times 10^{-3}$
mcOPO-Full	46.43	$3.79 \times 10^{-1}$	27.29	$2.12 \times 10^{-3}$
TAE	25.68	$2.14 \times 10^{-3}$	24.54	$1.49 \times 10^{-3}$
TAE-Full	25.68	$2.10 \times 10^{-3}$	24.54	$1.45 \times 10^{-3}$
Tik	22.71		22.71	

**Generating train and test data sets.** To generate data pairs of  $(\mathbf{u}, \omega)$ , we draw samples of  $u(x)$  using the truncated Karhunen-Loève expansion

$$(3.6) \quad u(x) = \sum_{i=1}^{24} \sqrt{\lambda_i} \phi_i(x) z_i,$$

where  $z_i \sim \mathcal{N}(0, 1)$ ,  $i = 1, \dots, 24$ , and  $(\lambda_i, \phi_i)$  are eigenpairs obtained by the eigendecomposition of the covariance operator  $7^{\frac{3}{2}} (-\Delta + 49\mathbf{I})^{-2.5}$  with periodic boundary conditions. Next, we discretize the initial vorticity  $u(x)$ , denoted as  $\mathbf{u}$ , and we solve the Navier-Stokes equation by the stream-function formulation with a pseudospectral method [47] to obtain a discrete

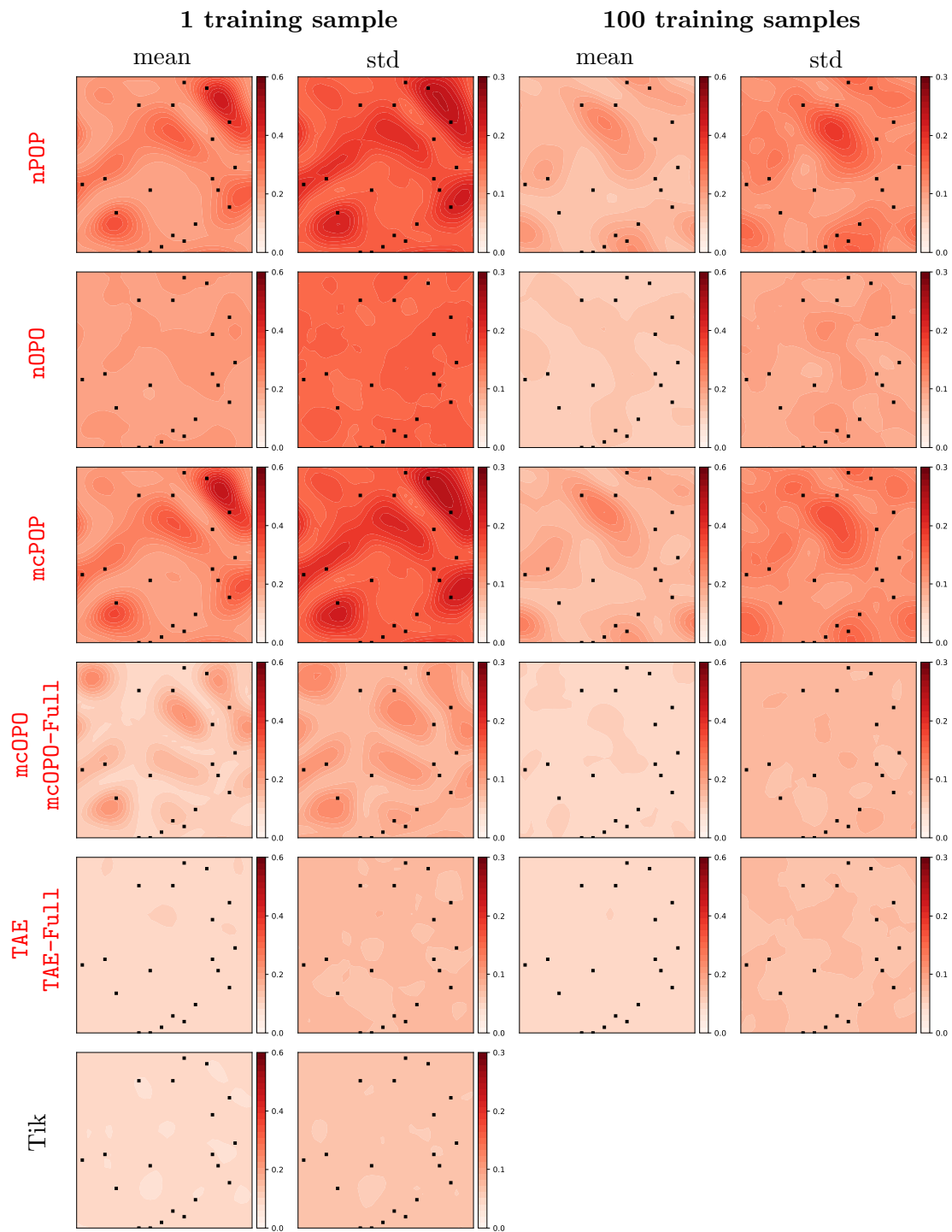


Figure 10: **2D Navier–Stokes equation.** Mean and standard deviation of absolute error of 500 test inverse solutions obtained from different approaches. Black points are observation locations.

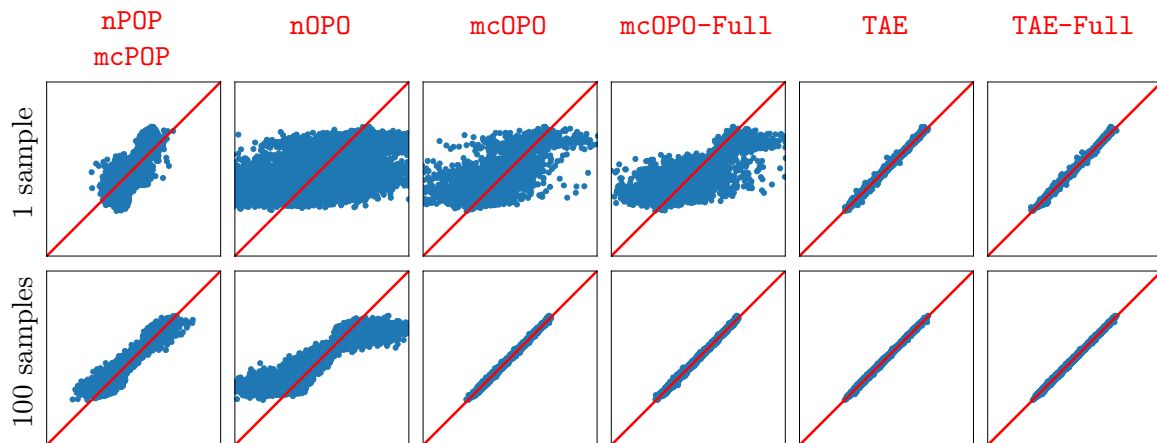


Figure 11: **2D Navier–Stokes equation.** The comparison of 500 test predicted observations obtained from different approaches. The red line indicates the perfect matching between predictions and the ground truth observation data set. **Top row:** Trained with 1 training sample. **Bottom row:** Trained with 100 training samples. In all plots plot, the x-axis is the magnitude of the true observation, and the y-axis is the magnitude of the predicted observation, both axes have a range of  $[-3, 3]$ .

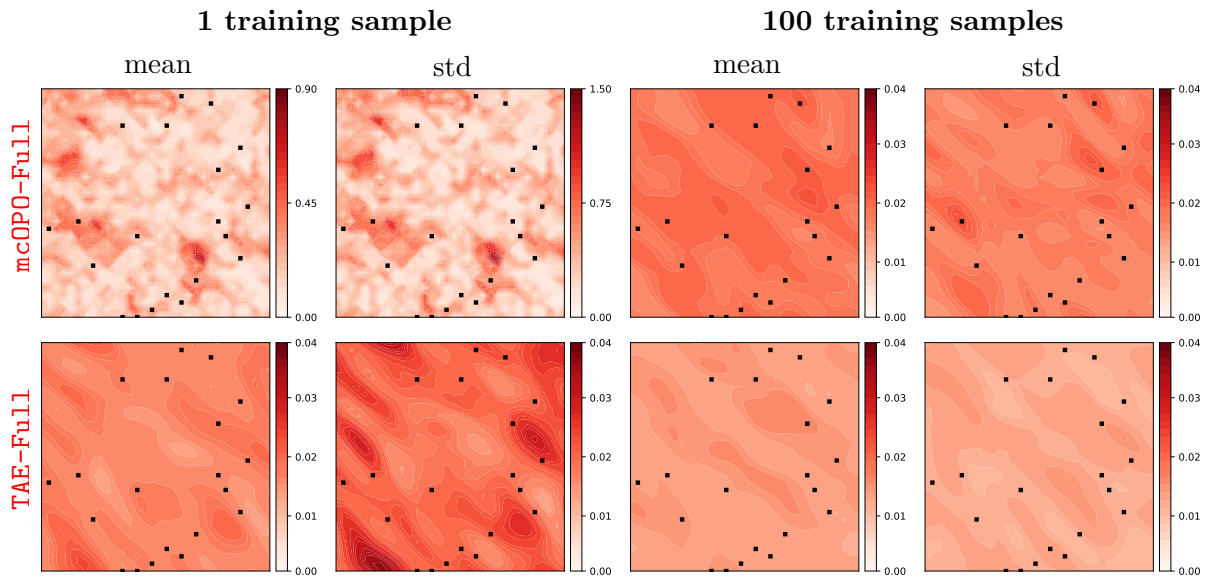


Figure 12: **2D Navier–Stokes equation.** Mean and standard deviation of absolute error of 500 test vorticity solutions at  $T = 10$  obtained from **mcOPO-Full** and **TAE-Full**. Black points are observation locations.

representation  $\omega$  of  $\omega(x, t)$  at time  $t = 10$ . The observation data  $\mathbf{y}$  is constructed by extracting the vorticity field  $\omega$  at  $T = 10$  at 20 randomly distributed observation locations, with the subsequent addition of  $\delta = 2\%$  Gaussian noise. Following this methodology, two distinct datasets are generated: a training set comprising 100 independent samples and a test set containing 500 samples. [Figure 9](#) illustrates the first sample pair from the training dataset of 100 samples, which serves as the training sample for single-sample training scenarios across all approaches.

**Learned inverse and PtO/forward maps accuracy.** Following the same procedure used for the 2D Poisson equation, encoder and decoder networks are trained sequentially for two cases: using a single training sample pair (shown in [Figure 9](#)) and using 100 training sample pairs. For [mcOPO](#), [mcOPO-Full](#), [TAE](#) and [TAE-Full](#) approaches, random realizations drawn with noise level  $\varepsilon = 25\%$  are added at each epoch during training to impose the data randomization technique. [Table 4](#) presents the relative errors of inverse and PtO/forward solutions computed from 500 test samples for all approaches.

When trained on a single sample, [TAE](#) and [TAE-Full](#) achieve the lowest relative error of 25.68% for inverse solutions among all approaches. Similarly, their PtO/forward solutions demonstrate superior accuracy with relative errors of  $2.14 \times 10^{-3}$  and  $2.10 \times 10^{-3}$ , respectively. This enhanced performance results from the combination of data randomization and forward solver model-constrained terms, enabling great generalization to unseen test samples. The [mcOPO](#) and [mcOPO-Full](#) approaches achieve second-best accuracy for inverse solutions with a relative error of 46.43%. This reduced accuracy stems from a strong bias toward the single training sample, despite the forward solver constraint, as detailed in [subsection 2.3.2](#). In contrast, [mcPOP](#), [nOPO](#), and [nPOP](#) exhibit significantly higher relative errors of 161.48%, 103.94%, and 156.99% respectively for inverse solutions. These poor results are expected for [nOPO](#) and [nPOP](#) due to their purely data-driven nature, thus limiting generalization. For [mcPOP](#), the inaccurate encoder (learned PtO map) propagates errors to the decoder training, resulting in imprecise inverse surrogate models. Regarding PtO/forward solutions, [nPOP](#), [nOPO](#), [mcPOP](#), [mcOPO](#), and [mcOPO-Full](#) fail to produce accurate surrogate models, reflecting overfitting to the single training sample despite forward solver regularization in the latter three approaches.

Training with 100 samples demonstrates significant accuracy improvements across all approaches for both inverse and PtO/forward surrogate models. It is expected as a result of the increase in the provided training information. The [TAE](#) and [TAE-Full](#) frameworks maintain superior performance, achieving relative errors of 24.54% for inverse solutions compared to the Tikhonov method benchmark of 22.71%. Their PtO/forward solutions exhibit good accuracy with relative errors of  $1.49 \times 10^{-3}$  and  $1.45 \times 10^{-3}$ , respectively. In the meantime, the relative error of the inverse solution obtained by [mcOPO](#) and [mcOPO-Full](#) is 27.29%, which is the second best among all approaches. The relative error of the PtO/forward solution obtained by [mcOPO](#) and [mcOPO-Full](#) is  $2.20 \times 10^{-3}$  and  $2.12 \times 10^{-3}$ , respectively, which is almost as good as [TAE](#) and [TAE-Full](#). This indicates the roles of model-constrained terms in reducing the overfitting effect as sufficient training data is provided. In contrast, [nPOP](#) and [mcPOP](#) exhibit substantially higher relative errors of 72.22% and 76.33%, respectively, for inverse solutions. These high error rates stem from inaccuracies in their pre-trained PtO map (encoder), consistent with observations from the single-sample training scenario. Meanwhile, [nOPO](#) framework shows improved inverse solution accuracy with a relative error of 40.20%, yet remains less accurate

than the model-constrained approaches (`mcOPO`, `mcOPO-Full`, `TAE`, and `TAE-Full`). This reduced performance gap aligns with the error factor analysis for linear problems, discussed in [subsection 2.3](#). Moreover, `nOPO`'s PtO solution accuracy remains notably poor ( $5.94 \times 10^{-1}$ ) despite the expanded training dataset, reflecting the inherent PtO mapping errors analyzed in [subsection 2.2.2](#). On the other hand, it is challenging to achieve inverse solutions as good as the Tikhonov regularization framework with `TAE` and `TAE-Full`. One possible reason is due to the high nonlinearity level of the Navier-Stokes equation forward map of which the inverse map is not easily approximated well by a neural network.

We further elaborate on the accuracy of forward and inverse surrogate models obtained from all approaches. [Figure 3](#) illustrates the spatial distribution of error statistics, presenting both mean and standard deviation of absolute errors between predicted and ground truth inverse solutions across 500 test cases for all approaches. The `TAE` and `TAE-Full` frameworks demonstrate superior performance, exhibiting the lowest mean and standard deviation of absolute errors across the domain for both single-sample and 100-sample training scenarios. The `mcOPO` and `mcOPO-Full` approaches achieve comparable accuracy only when trained with 100 samples, while their single-sample training results exhibit substantially high mean and standard deviation absolute error values. This performance difference underscores the enhanced generalization capabilities of the `TAE` and `TAE-Full` frameworks compared to their model-constrained counterparts, `mcOPO` and `mcOPO-Full`. In contrast, the `mcPOP`, `nPOP`, and `nOPO` approaches consistently demonstrate significantly higher mean and standard deviation of absolute errors across the domain in both training scenarios.

In the meantime, [Figure 11](#) presents a quantitative comparison between predicted observations and ground truth across different approaches. In the single-sample training scenario, only `TAE` and `TAE-Full` demonstrate accurate observation predictions, while other approaches exhibit substantial deviations from ground truth values. With the expanded 100-sample training dataset, `mcOPO` and `mcOPO-Full` join `TAE` and `TAE-Full` in achieving significant improvements in observation and vorticity field predictions. However, `nPOP`, `nOPO`, and `mcPOP` continue to produce inaccurate predictions even with increased training data. The capability of `TAE-Full` and `mcOPO-Full` to function as direct surrogate solvers for the Navier-Stokes equation merits particular attention. [Figure 12](#) illustrates the spatial distribution of error statistics, showing the mean and standard deviation of absolute errors between predicted and true vorticity fields across 500 test samples. In the single-sample training scenario, `mcOPO-Full` exhibits substantial prediction errors, while `TAE-Full` maintains pretty good accuracy in vorticity field predictions. The transition to 100-sample training yields marked accuracy improvements for both frameworks in vorticity field predictions, demonstrating their potential as efficient surrogate solvers when provided with sufficient training data.

**TAE-Full is the best for learning both inverse and forward surrogate models.**

Analogous to the heat equation findings in [subsection 3.1](#), `TAE-Full` framework demonstrates superior performance in learning both inverse solvers and forward surrogate models for PDE solutions. Predicted initial vorticity field test samples obtained by `TAE-Full` trained with one training sample and Tikhonov regularization framework is shown in [Figure 13](#). The `TAE-Full` inverse solution exhibits strong concordance with the Tikhonov regularization solution, closely approximating the ground truth vorticity field. Furthermore, [Figure 6](#) demonstrates that the `TAE-Full` predicted vorticity field at final time  $T = 10$  achieves remarkable agreement with

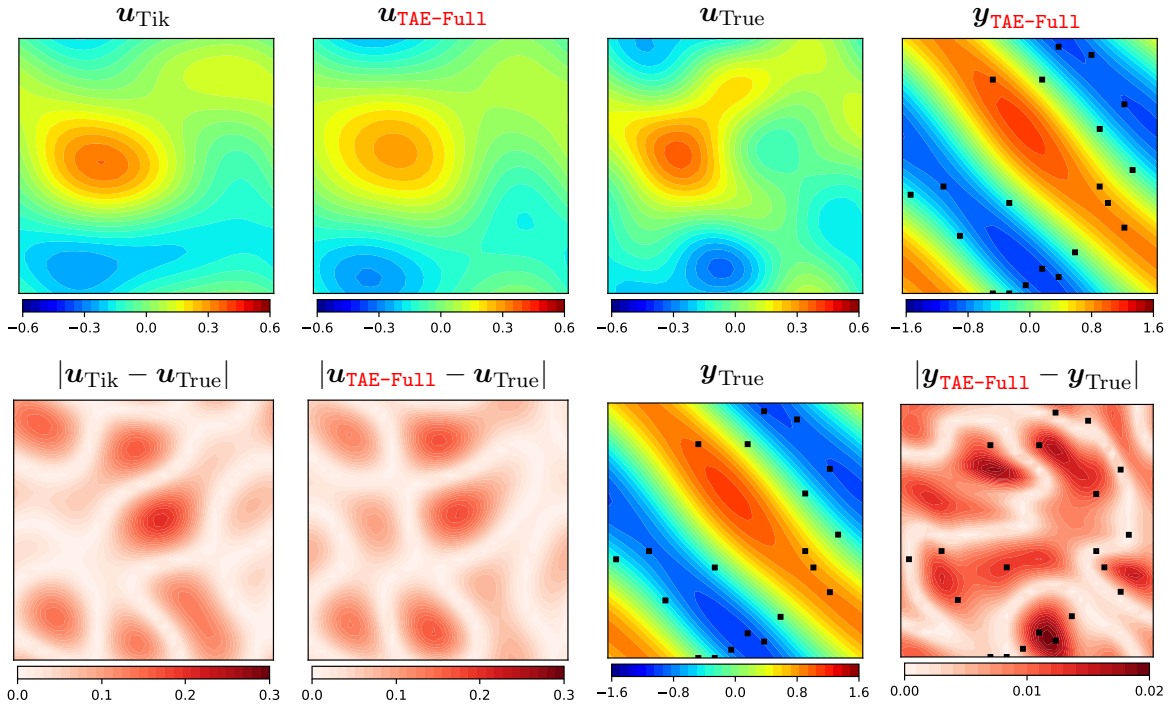


Figure 13: **2D Navier–Stokes equation.** A sample of inverted initial vorticity field and final time  $T = 10$  vorticity field obtained by **TAE-Full** trained with 1 training sample coupled with data randomization of noise level  $\sigma = 0.25$ .

the ground truth distribution. The spatial distribution of absolute errors for both initial and final time vorticity fields reveals small discrepancies from true values. It is important to note that the single training data pair, as shown in Figure 9, is completely different from the shown test sample under consideration. This observation demonstrates a great generalization capacity of **TAE-Full** framework to unseen test samples.

**TAE-Full robustness to a wide range of noise levels.** A survey of **TAE-Full** trained with one training sample over a wide range of noise levels is shown in Figure 14. The framework exhibits remarkable stability in inverse solution accuracy within noise levels ranging from  $\varepsilon \in [0.15, 0.5]$ , demonstrating robust performance over a wide range of noise spectrum. Performance degradation is observed outside of the optimal noise level range. At low noise levels, the data randomization process provides insufficient variation to effectively explore the space of unseen test samples, limiting the framework’s ability to leverage forward solver constraints. Conversely, excessive noise levels result in training data becoming statistically indistinguishable, degenerating the framework’s capacity to learn accurate inverse mappings.

**TAE-Full robustness to arbitrary individual samples for single-sample training case.** The robustness of **TAE-Full** to arbitrary individual training samples is examined. To be more specific, we randomly pick 12 samples out of 100 training sample data sets. The indices of 20 random observation locations are presented in the left figure in Figure 15. Meanwhile,



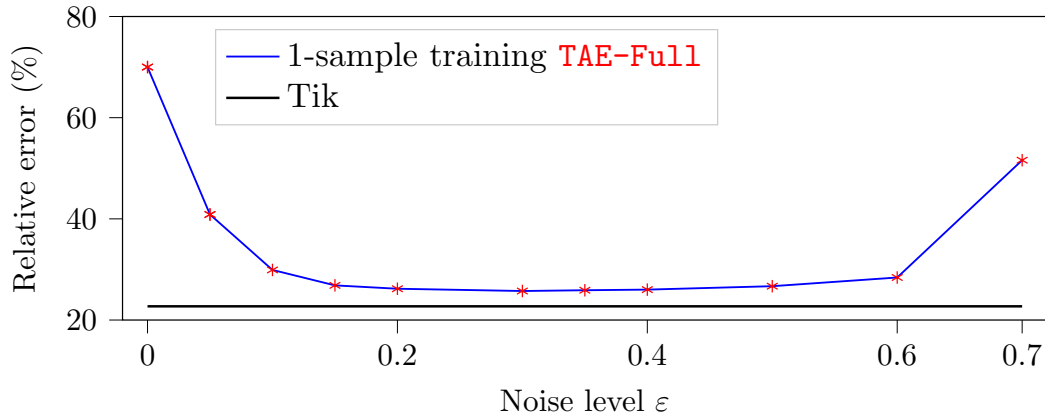


Figure 14: **2D Navier–Stokes equation.** Relative error of inverse solution over 500 test samples with different noise levels  $\varepsilon$ .

the mean and standard deviation of observation magnitudes of 10000 true observation samples at corresponding 20 random observation locations and the observation magnitudes of 12 different observation samples under consideration for single-sample training cases are shown in Figure 15. From 12 corresponding single-sample training cases, we obtain the mean and standard deviation of the relative error of the inverse solution is  $25.88 \pm 0.19\%$ . This marginal relative error standard deviation demonstrates the **TAE-Full** framework’s independence from the choice of which individual sample in single-sample training scenarios.

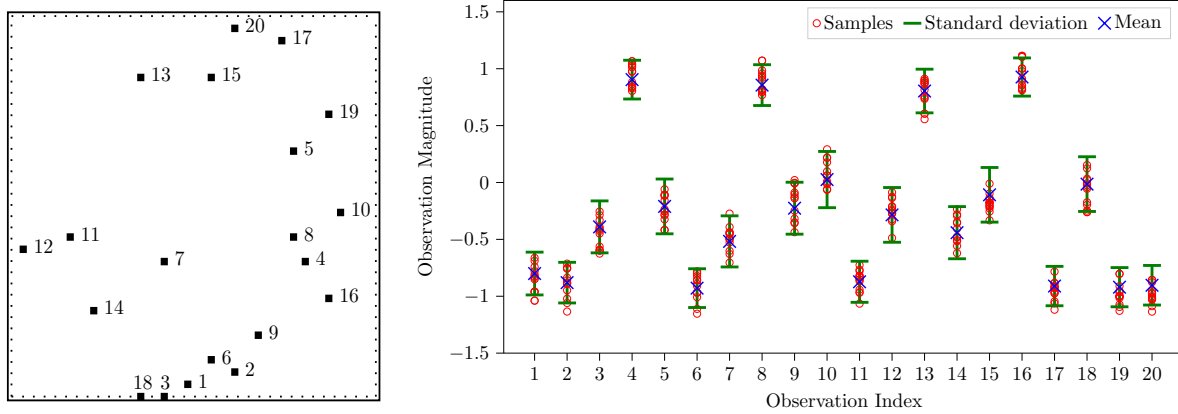


Figure 15: **2D Navier–Stokes equation.** **Left:** Index of 20 observation locations. **Right:** Mean and standard deviation of observation magnitudes of 10000 true observation samples at observation locations. And, the observation magnitudes of 12 different observation samples for single-sample training cases.

Table 5: The training cost (measured in hours) for the case of  $n_t = 100$  randomized training samples for Heat and Navier–Stokes equation problems. The computational time (measured in seconds) for forward and inverse solution governed by heat equation and Navier-Stokes equation using **TAE-Full** and numerical solvers, and the speed-up (fourth row) of **TAE-Full** relative to numerical solvers using NVIDIA A100 GPUs on Lonestar6 at the Texas Advanced Computing Center (TACC).

		Heat equation	Navier–Stokes
Training Encoder + Training Decoder (hours)		2	16
Test/Inference (second)	Inverse (Encoder)	$2.74 \times 10^{-4}$	$2.93 \times 10^{-4}$
	Forward (Decoder)	$2.86 \times 10^{-4}$	$3.06 \times 10^{-4}$
Numerical solvers (second)	Inverse (Tikhonov)	$4.36 \times 10^{-2}$	7.26
	Forward	$3.01 \times 10^{-2}$	0.38
Speed up	Inverse	159	<b>24,785</b>
	Forward	105	<b>1,241</b>

**3.3. Training cost and speedup with deep learning solutions.** The training costs for the case of  $n_t = 100$  randomized training samples for inverse heat conductivity and Navier–Stokes equations are presented in Table 5. It can be observed that the heat equation requires a small amount of training time, about 2 hours, while the corresponding time for the Navier–Stokes equations is about 16 hours. It should be noted that executing the forward map and the backpropagation constitutes the majority of the training cost. Table 5 also provides information on the computational cost of reconstructing PoIs given an unseen test observation sample and solving for PDE solutions given an unseen PoI sample. To be more specific, for inverse solutions, we use the classical Tikhonov (TIK) regularization technique and our proposed deep learning approach **TAE-Full** using the encoder network. In contrast, we use numerical methods and **TAE-Full** decoder for forward PDEs solutions. It can be seen that the training, and test computational time depends on the complexity of problems. We note that the complexity is estimated based on the number of time steps, the operations carried out per time step, and the mesh size. As can be seen, the more complicated the problem is, the more time Tikhonov and numerical solvers take to obtain the inverse and forward solutions, respectively. Unlike the Tikhonov approach, regardless of the complexity of the problems, the learned **TAE-Full** encoder and decoder maps using one hidden layer with 5000 neurons takes the same small amount of time: approximately 0.0003 seconds. Note that the Tikhonov solver is implemented directly in JAX using the default BFGS algorithm with the gradient computed by the default Autograd functionality. Thus, the Tikhonov computation enjoys JAX optimized features including XLA (accelerated linear algebra), JIT (just-in-time compilation), and the nested primitive loop technique. In the meantime, the majority of computational time for numerical forward solvers stems from JIT compiling the numerical solvers. JIT functionality takes a significant amount of time to cache the modular function for the first, then all following calls of the same function are significantly faster. This is why,

for simple problems such as the Heat equation, we observe a little difference between the forward solver and the Tikhonov solver which requires numerous forward solvers. Even with such optimization, numerical forward and Tikhonov solvers are still orders of magnitude slower than **TAE-Full** neural networks. In particular, for the Navier-Stokes equation, **TAE-Full** is 24,785 times faster than Tikhonov and 1,241 times faster than the numerical forward solver using the spectral method. We expect the computational gain to be more significant for larger-scale 3D time-dependent nonlinear forward problems. Clearly, once trained, obtaining **TAE-Full** solutions is simply a feed-forward neural network evaluation, which could be close to real-time or real-time depending on the network’s depth and the width.

**4. Conclusion.** This paper presents a Tikhonov autoencoder model-constrained machine learning framework, called **TAE**, for solving forward and inverse problems. A comprehensive error estimation analysis across pure data-driven, model-constrained, and Tikhonov model-constrained approaches is provided. Among approaches, **TAE** and its variant **TAE-Full** uniquely achieve both the exact Tikhonov solver and exact PtO map/forward map using an arbitrary observation sample. This beauty stems from incorporating the data randomization strategy with a proper noise level within the model-constrained framework. Additionally, we establish theoretical support for sequential encoder-decoder training over simultaneous optimization. Numerical experiments on 2D heat equation and 2D Navier-Stokes equations validate these theoretical findings, demonstrating that **TAE** and **TAE-Full** solutions achieve accuracy comparable to Tikhonov solutions for inverse problems and numerical forward solver solutions for forward problems while delivering computational speedups of several orders of magnitude, using only one arbitrary observation sample. Ongoing work focuses on extending the **TAE** framework to variable-observation inverse problems, where we anticipate developing encoders adaptable to diverse observation scenarios (varying measurement locations and quantities) while maintaining accurate PtO map/forward map representation through the decoder. Future work will explore extensions to statistical inversions. While **TAE**’s primary limitation—the requirement for a differentiable solver during training—can be addressed through differential numerical libraries or by substituting differential residual evaluation for the differentiable solver, these developments will be detailed in subsequent publications.

**Acknowledgments.** The authors would like to thank Arjit Seth, Krishnanunni Chandradath Girija, and Wesley Lao for fruitful discussions. The authors also acknowledge the Texas Advanced Computing Center (TACC) at The University of Texas at Austin for providing HPC, visualization, database, or grid resources that have contributed to the research results reported within this paper. URL: <http://www.tacc.utexas.edu>

## REFERENCES

- [1] Hemant K Aggarwal, Merry P Mani, and Mathews Jacob. Modl: Model-based deep learning architecture for inverse problems. *IEEE transactions on medical imaging*, 38(2):394–405, 2018.
- [2] Manal Almaeen, Yasir Alanazi, Nobuo Sato, W Melnitchouk, Michelle P Kuchera, and Yaohang Li. Variational autoencoder inverse mapper: An end-to-end deep learning framework for inverse problems. In *2021 International Joint Conference on Neural Networks (IJCNN)*, pages 1–8. IEEE, 2021.
- [3] Simon Arridge, Peter Maass, Ozan Öktem, and Carola-Bibiane Schönlieb. Solving inverse problems using data-driven models. *Acta Numerica*, 28:1–174, 2019.

- [4] Mark Austin, Parastoo Delgoshaei, Maria Coelho, and Mohammad Heidarinejad. Architecting smart city digital twins: Combined semantic model and machine learning approach. *Journal of Management in Engineering*, 36(4):04020026, 2020.
- [5] Shivam Barwey and Romit Maulik. Interpretable fine-tuning for graph neural network surrogate models. *arXiv preprint arXiv:2311.07548*, 2023.
- [6] Jens Berg and Kaj Nyström. Neural network augmented inverse problems for pdes. *arXiv preprint arXiv:1712.09685*, 2017.
- [7] Chris M Bishop. Training with noise is equivalent to tikhonov regularization. *Neural computation*, 7(1):108–116, 1995.
- [8] Yoeri E Boink and Christoph Brune. Learned svd: solving inverse problems via hybrid autoencoding. *arXiv preprint arXiv:1912.10840*, 2019.
- [9] James Bradbury, Roy Frostig, Peter Hawkins, Matthew James Johnson, Chris Leary, Dougal Maclaurin, George Necula, Adam Paszke, Jake VanderPlas, Skye Wanderman-Milne, and Qiao Zhang. JAX: composable transformations of Python+NumPy programs, 2018.
- [10] Shengze Cai, Zhicheng Wang, Sifan Wang, Paris Perdikaris, and George Em Karniadakis. Physics-informed neural networks for heat transfer problems. *Journal of Heat Transfer*, 143(6):060801, 2021.
- [11] Min Chen, Xiaobo Shi, Yin Zhang, Di Wu, and Mohsen Guizani. Deep feature learning for medical image analysis with convolutional autoencoder neural network. *IEEE Transactions on Big Data*, 7(4):750–758, 2017.
- [12] Nan-Chen Chen, Margaret Drouhard, Rafal Kocielnik, Jina Suh, and Cecilia R Aragon. Using machine learning to support qualitative coding in social science: Shifting the focus to ambiguity. *ACM Transactions on Interactive Intelligent Systems (TüS)*, 8(2):1–20, 2018.
- [13] Ricky TQ Chen, Yulia Rubanova, Jesse Bettencourt, and David K Duvenaud. Neural ordinary differential equations. *Advances in neural information processing systems*, 31, 2018.
- [14] Yuyao Chen, Lu Lu, George Em Karniadakis, and Luca Dal Negro. Physics-informed neural networks for inverse problems in nano-optics and metamaterials. *Optics express*, 28(8):11618–11633, 2020.
- [15] Matthias Chung, Emma Hart, Julianne Chung, Bas Peters, and Eldad Haber. Paired autoencoders for inverse problems. *arXiv preprint arXiv:2405.13220*, 2024.
- [16] Paul G Constantine, Carson Kent, and Tan Bui-Thanh. Accelerating markov chain monte carlo with active subspaces. *SIAM Journal on Scientific Computing*, 38(5):A2779–A2805, 2016.
- [17] Salvatore Cuomo, Vincenzo Schiano Di Cola, Fabio Giampaolo, Gianluigi Rozza, Maziar Raissi, and Francesco Piccialli. Scientific machine learning through physics-informed neural networks: Where we are and what’s next. *Journal of Scientific Computing*, 92(3):88, 2022.
- [18] Jia Deng, Wei Dong, Richard Socher, Li-Jia Li, Kai Li, and Li Fei-Fei. Imagenet: A large-scale hierarchical image database. In *2009 IEEE conference on computer vision and pattern recognition*, pages 248–255. Ieee, 2009.
- [19] Harris Drucker and Yann Le Cun. Improving generalization performance using double backpropagation. *IEEE transactions on neural networks*, 3(6):991–997, 1992.
- [20] Robert Eymard, Thierry Gallouët, and Raphaële Herbin. Finite volume methods. *Handbook of numerical analysis*, 7:713–1018, 2000.
- [21] Tiffany Fan, Kailai Xu, Jay Pathak, and Eric Darve. Solving inverse problems in steady-state navier-stokes equations using deep neural networks. *arXiv preprint arXiv:2008.13074*, 2020.
- [22] Xinlong Feng and Zhinan Zhang. The rank of a random matrix. *Applied Mathematics and Computation*, 185(1):689–694, 2007.
- [23] Chris Finlay and Adam M Oberman. Scaleable input gradient regularization for adversarial robustness. *Machine Learning with Applications*, 3:100017, 2021.
- [24] Ken-ichi Funahashi and Yuichi Nakamura. Approximation of dynamical systems by continuous time recurrent neural networks. *Neural networks*, 6(6):801–806, 1993.
- [25] Nicholas Geneva and Nicholas Zabaras. Transformers for modeling physical systems. *Neural Networks*, 146:272–289, 2022.
- [26] Sergei K Godunov and I Bohachevsky. Finite difference method for numerical computation of discontinuous solutions of the equations of fluid dynamics. *Matematicheskij sbornik*, 47(3):271–306, 1959.
- [27] Hwan Goh, Sheroze Sherifdeen, Jonathan Wittmer, and Tan Bui-Thanh. Solving bayesian inverse problems via variational autoencoders. *arXiv preprint arXiv:1912.04212*, 2019.

- [28] Gene H Golub, Per Christian Hansen, and Dianne P O’Leary. Tikhonov regularization and total least squares. *SIAM journal on matrix analysis and applications*, 21(1):185–194, 1999.
- [29] Lovedeep Gondara. Medical image denoising using convolutional denoising autoencoders. In *2016 IEEE 16th international conference on data mining workshops (ICDMW)*, pages 241–246. IEEE, 2016.
- [30] Francisco J Gonzalez and Maciej Balajewicz. Deep convolutional recurrent autoencoders for learning low-dimensional feature dynamics of fluid systems. *arXiv preprint arXiv:1808.01346*, 2018.
- [31] Ronald B Guenther and John W Lee. *Partial differential equations of mathematical physics and integral equations*. Courier Corporation, 1996.
- [32] Kaiming He, Xinlei Chen, Saining Xie, Yanghao Li, Piotr Dollár, and Ross Girshick. Masked autoencoders are scalable vision learners. In *Proceedings of the IEEE/CVF conference on computer vision and pattern recognition*, pages 16000–16009, 2022.
- [33] Kazufumi Ito and Bangti Jin. *Inverse problems: Tikhonov theory and algorithms*, volume 22. World Scientific, 2014.
- [34] Ameya D Jagtap, Ehsan Kharazmi, and George Em Karniadakis. Conservative physics-informed neural networks on discrete domains for conservation laws: Applications to forward and inverse problems. *Computer Methods in Applied Mechanics and Engineering*, 365:113028, 2020.
- [35] Ameya D Jagtap, Zhiping Mao, Nikolaus Adams, and George Em Karniadakis. Physics-informed neural networks for inverse problems in supersonic flows. *Journal of Computational Physics*, 466:111402, 2022.
- [36] Yuchen Jin, Qiuyang Shen, Xuqing Wu, Jiefu Chen, and Yueqin Huang. A physics-driven deep-learning network for solving nonlinear inverse problems. *Petrophysics*, 61(01):86–98, 2020.
- [37] Zhaoyang Larry Jin, Yimin Liu, and Louis J Durlofsky. Deep-learning-based surrogate model for reservoir simulation with time-varying well controls. *Journal of Petroleum Science and Engineering*, 192:107273, 2020.
- [38] Jari Kaipio and Erkki Somersalo. *Statistical and computational inverse problems*, volume 160. Springer Science & Business Media, 2006.
- [39] Diederik P Kingma and Jimmy Ba. Adam: A method for stochastic optimization. *arXiv preprint arXiv:1412.6980*, 2014.
- [40] Alex Krizhevsky, Ilya Sutskever, and Geoffrey E Hinton. Imagenet classification with deep convolutional neural networks. *Advances in neural information processing systems*, 25, 2012.
- [41] Chao-Chee Ku and Kwang Y Lee. Diagonal recurrent neural networks for dynamic systems control. *IEEE transactions on neural networks*, 6(1):144–156, 1995.
- [42] Kookjin Lee and Kevin T Carlberg. Model reduction of dynamical systems on nonlinear manifolds using deep convolutional autoencoders. *Journal of Computational Physics*, 404:108973, 2020.
- [43] Randall J LeVeque. *Finite volume methods for hyperbolic problems*, volume 31. Cambridge university press, 2002.
- [44] Housen Li, Johannes Schwab, Stephan Antholzer, and Markus Haltmeier. Nett: Solving inverse problems with deep neural networks. *Inverse Problems*, 36(6):065005, 2020.
- [45] Zijie Li, Kazem Meidani, and Amir Barati Farimani. Transformer for partial differential equations’ operator learning. *arXiv preprint arXiv:2205.13671*, 2022.
- [46] Zongyi Li, Nikola Kovachki, Kamyar Azizzadenesheli, Burigede Liu, Kaushik Bhattacharya, Andrew Stuart, and Anima Anandkumar. Fourier neural operator for parametric partial differential equations. *arXiv preprint arXiv:2010.08895*, 2020.
- [47] Zongyi Li, Nikola Kovachki, Kamyar Azizzadenesheli, Burigede Liu, Kaushik Bhattacharya, Andrew Stuart, and Anima Anandkumar. Fourier neural operator for parametric partial differential equations, 2020.
- [48] Dianjing Liu, Yixuan Tan, Erfan Khoram, and Zongfu Yu. Training deep neural networks for the inverse design of nanophotonic structures. *Acs Photonics*, 5(4):1365–1369, 2018.
- [49] Lu Lu, Pengzhan Jin, Guofei Pang, Zhongqiang Zhang, and George Em Karniadakis. Learning nonlinear operators via deepnet based on the universal approximation theorem of operators. *Nature machine intelligence*, 3(3):218–229, 2021.
- [50] Sebastian Lunz, Ozan Öktem, and Carola-Bibiane Schönlieb. Adversarial regularizers in inverse problems. *Advances in neural information processing systems*, 31, 2018.
- [51] Kiyotoshi Matsuoka. Noise injection into inputs in back-propagation learning. *IEEE Transactions on*

- Systems, Man, and Cybernetics*, 22(3):436–440, 1992.
- [52] Nima Mohajerin and Steven L Waslander. Multistep prediction of dynamic systems with recurrent neural networks. *IEEE transactions on neural networks and learning systems*, 30(11):3370–3383, 2019.
  - [53] Beatriz Moya, Alberto Badiás, Iciar Alfaro, Francisco Chinesta, and Elías Cueto. Digital twins that learn and correct themselves. *International Journal for Numerical Methods in Engineering*, 123(13):3034–3044, 2022.
  - [54] Hai Nguyen, Jonathan Wittmer, and Tan Bui-Thanh. Dias: a data-informed active subspace regularization framework for inverse problems. *Computation*, 10(3):38, 2022.
  - [55] Hai V Nguyen and Tan Bui-Thanh. A model-constrained tangent slope learning approach for dynamical systems. *International Journal of Computational Fluid Dynamics*, 36(7):655–685, 2022.
  - [56] Hai V Nguyen and Tan Bui-Thanh. Tnet: A model-constrained tikhonov network approach for inverse problems. *SIAM Journal on Scientific Computing*, 46(1):C77–C100, 2024.
  - [57] Jorge Nocedal and Stephen J Wright. *Numerical optimization*. Springer, 1999.
  - [58] Thomas O’Leary-Roseberry, Peng Chen, Umberto Villa, and Omar Ghattas. Derivative-informed neural operator: an efficient framework for high-dimensional parametric derivative learning. *Journal of Computational Physics*, 496:112555, 2024.
  - [59] Gregory Ongie, Ajil Jalal, Christopher A Metzler, Richard G Baraniuk, Alexandros G Dimakis, and Rebecca Willett. Deep learning techniques for inverse problems in imaging. *IEEE Journal on Selected Areas in Information Theory*, 1(1):39–56, 2020.
  - [60] M Necati Özişik, Helcio RB Orlande, Marcelo J Colaço, and Renato M Cotta. *Finite difference methods in heat transfer*. CRC press, 2017.
  - [61] Thomas O’Leary-Roseberry, Umberto Villa, Peng Chen, and Omar Ghattas. Derivative-informed projected neural networks for high-dimensional parametric maps governed by pdes. *Computer Methods in Applied Mechanics and Engineering*, 388:114199, 2022.
  - [62] Samira Pakravan, Pouria A Mistani, Miguel A Aragon-Calvo, and Frederic Gibou. Solving inverse-pde problems with physics-aware neural networks. *Journal of Computational Physics*, 440:110414, 2021.
  - [63] Shaowu Pan and Karthik Duraisamy. Long-time predictive modeling of nonlinear dynamical systems using neural networks. *Complexity*, 2018, 2018.
  - [64] Robert L Parker. *Geophysical inverse theory*, volume 1. Princeton university press, 1994.
  - [65] Nicholas Perrone and Robert Kao. A general finite difference method for arbitrary meshes. *Computers & Structures*, 5(1):45–57, 1975.
  - [66] Federico Pichi, Beatriz Moya, and Jan S Hesthaven. A graph convolutional autoencoder approach to model order reduction for parametrized pdes. *Journal of Computational Physics*, 501:112762, 2024.
  - [67] Tomaso Poggio and Federico Girosi. Networks for approximation and learning. *Proceedings of the IEEE*, 78(9):1481–1497, 1990.
  - [68] Maziar Raissi, Paris Perdikaris, and George E Karniadakis. Physics-informed neural networks: A deep learning framework for solving forward and inverse problems involving nonlinear partial differential equations. *Journal of Computational Physics*, 378:686–707, 2019.
  - [69] Singiresu S Rao. *The finite element method in engineering*. Elsevier, 2010.
  - [70] M Mazhar Rathore, Syed Attique Shah, Dharendra Shukla, Elmahdi Bentafat, and Spiridon Bakiras. The role of ai, machine learning, and big data in digital twinning: A systematic literature review, challenges, and opportunities. *IEEE Access*, 9:32030–32052, 2021.
  - [71] JN Reddy. An introduction to the finite element method, 1993.
  - [72] Russell Reed, Seho Oh, RJ Marks, et al. Regularization using jittered training data. In *International Joint Conference on Neural Networks*, volume 3, pages 147–152, 1992.
  - [73] Yaniv Romano, Michael Elad, and Peyman Milanfar. The little engine that could: Regularization by denoising (red). *SIAM Journal on Imaging Sciences*, 10(4):1804–1844, 2017.
  - [74] Andrew Ross and Finale Doshi-Velez. Improving the adversarial robustness and interpretability of deep neural networks by regularizing their input gradients. In *Proceedings of the AAAI conference on artificial intelligence*, volume 32, 2018.
  - [75] Alvaro Sanchez-Gonzalez, Jonathan Godwin, Tobias Pfaff, Rex Ying, Jure Leskovec, and Peter Battaglia. Learning to simulate complex physics with graph networks. In *International Conference on Machine Learning*, pages 8459–8468. PMLR, 2020.
  - [76] Anand Pratap Singh, Shivaaji Medida, and Karthik Duraisamy. Machine-learning-augmented predictive

- modeling of turbulent separated flows over airfoils. *AIAA journal*, 55(7):2215–2227, 2017.
- [77] Vincent Sitzmann, Julien Martel, Alexander Bergman, David Lindell, and Gordon Wetzstein. Implicit neural representations with periodic activation functions. *Advances in neural information processing systems*, 33:7462–7473, 2020.
- [78] Arnold Sommerfeld. *Partial differential equations in physics*. Academic press, 1949.
- [79] Jian Sun, Kristopher Innanen, Tianze Zhang, and Daniel Trad. Implicit seismic full waveform inversion with deep neural representation. *Journal of Geophysical Research: Solid Earth*, 128(3):e2022JB025964, 2023.
- [80] Albert Tarantola. *Inverse problem theory and methods for model parameter estimation*. SIAM, 2005.
- [81] Hai Van Nguyen, Jau-Uei Chen, William Cole Nockolds, Wesley Lao, and Tan Bui-Thanh. A model-constrained discontinuous galerkin network (dgnnet) for compressible euler equations with out-of-distribution generalization. *arXiv preprint arXiv:2409.18371*, 2024.
- [82] A Vaswani. Attention is all you need. *Advances in Neural Information Processing Systems*, 2017.
- [83] Curtis R Vogel. *Computational methods for inverse problems*. SIAM, 2002.
- [84] Zhong Yi Wan, Leonardo Zepeda-Nunez, Anudhyan Boral, and Fei Sha. Evolve smoothly, fit consistently: Learning smooth latent dynamics for advection-dominated systems. *arXiv preprint arXiv:2301.10391*, 2023.
- [85] Sifan Wang, Hanwen Wang, and Paris Perdikaris. Learning the solution operator of parametric partial differential equations with physics-informed deeponets. *Science advances*, 7(40):eabi8605, 2021.
- [86] Yi-Jen Wang and Chin-Teng Lin. Runge-kutta neural network for identification of dynamical systems in high accuracy. *IEEE Transactions on Neural Networks*, 9(2):294–307, 1998.
- [87] Yue Wu and Youzuo Lin. Inversionnet: A real-time and accurate full waveform inversion with cnns and continuous crfs. *arXiv preprint arXiv:1811.07875*, 2018.
- [88] Yiheng Xie, Towaki Takikawa, Shunsuke Saito, Or Litany, Shiqin Yan, Numair Khan, Federico Tombari, James Tompkin, Vincent Sitzmann, and Srinath Sridhar. Neural fields in visual computing and beyond. In *Computer Graphics Forum*, volume 41, pages 641–676. Wiley Online Library, 2022.
- [89] Jiayang Xu and Karthik Duraisamy. Multi-level convolutional autoencoder networks for parametric prediction of spatio-temporal dynamics. *Computer Methods in Applied Mechanics and Engineering*, 372:113379, 2020.
- [90] Jeremy Yu, Lu Lu, Xuhui Meng, and George Em Karniadakis. Gradient-enhanced physics-informed neural networks for forward and inverse pde problems. *Computer Methods in Applied Mechanics and Engineering*, 393:114823, 2022.
- [91] Kai Zhang, Wangmeng Zuo, Shuhang Gu, and Lei Zhang. Learning deep cnn denoiser prior for image restoration. In *Proceedings of the IEEE conference on computer vision and pattern recognition*, pages 3929–3938, 2017.
- [92] Michael S Zhdanov. *Geophysical inverse theory and regularization problems*, volume 36. Elsevier, 2002.
- [93] Qinyu Zhuang, Juan Manuel Lorenzi, Hans-Joachim Bungartz, and Dirk Hartmann. Model order reduction based on runge–kutta neural networks. *Data-Centric Engineering*, 2, 2021.

## 5. Appendix.

### 5.1. Derivation of $W_e, \mathbf{b}_e, W_d, \mathbf{b}_d$ for nOP0.

**Loss function:** We train the encoder and decoder sequentially. First, we train the encoder, given training data samples. Then, we train the decoder, given the pretrained encoder. The optimal solutions for this training strategy are derived as following. The loss function for the encoder is given as:

$$(5.1) \quad \mathcal{L}_e = \frac{1}{2} \|W_e Y + \mathbf{b}_e \mathbf{1}^T - U\|_F^2$$

For simplicity, let's denote  $Z = W_e Y + \mathbf{b}_e \mathbf{1}^T$ . Then, loss function for the decoder given a pre-trained encoder is:

$$(5.2) \quad \mathcal{L}_d = \frac{1}{2} \|W_d Z + \mathbf{b}_d \mathbf{1}^T - Y\|_F^2$$

**Zero gradients and solving:** To find the optimal values, we set all gradients to zero and solve the resulting system of equations:

- Gradient with respect to  $\mathbf{b}_e$

$$(5.3) \quad \frac{\partial \mathcal{L}_e}{\partial \mathbf{b}_e} = (W_e Y + \mathbf{b}_e \mathbf{1}^T - U) \mathbf{1} = (W_e Y + \mathbf{b}_e \mathbf{1}^T) \mathbf{1} - U \mathbf{1} = 0$$

Solving for  $\mathbf{b}_e$  we have:

$$(5.4) \quad \mathbf{b}_e = \frac{1}{n_t} (U \mathbf{1} - W_e Y \mathbf{1})$$

- Gradient with respect to  $W_e$

$$(5.5) \quad \frac{\partial \mathcal{L}_e}{\partial W_e} = (W_e Y + \mathbf{b}_e \mathbf{1}^T - U) Y^T = (W_e Y + \mathbf{b}_e \mathbf{1}^T) Y^T - U Y^T = 0$$

Solving for  $W_e$  we have:

$$(5.6) \quad \begin{aligned} W_e Y Y^T + \mathbf{b}_e \mathbf{1}^T Y^T - U Y^T &= 0 \\ W_e Y Y^T + \frac{1}{n_t} (U \mathbf{1} - W_e Y \mathbf{1}) \mathbf{1}^T Y^T - U Y^T &= 0 \\ W_e Y Y^T - W_e Y \frac{\mathbf{1} \mathbf{1}^T}{n_t} Y^T - U Y^T + U \frac{\mathbf{1} \mathbf{1}^T}{n_t} Y^T &= 0 \\ W_e \bar{Y} \bar{Y}^T - \bar{U} \bar{Y}^T &= 0 \\ W_e &= \bar{U} \bar{Y}^\dagger \end{aligned}$$



- Gradient with respect to  $\mathbf{b}_d$

$$(5.7) \quad \frac{\partial \mathcal{L}_d}{\partial \mathbf{b}_d} = (W_d Z + \mathbf{b}_d \mathbf{1}^T - Y) \mathbf{1} = W_d Z \mathbf{1} + n_t \mathbf{b}_d - Y \mathbf{1} = 0$$

Solving for  $\mathbf{b}_d$  we have:

$$(5.8) \quad \mathbf{b}_d = \frac{1}{n_t} (Y \mathbf{1} - W_d Z \mathbf{1})$$

- Gradient with respect to  $W_d$

$$(5.9) \quad \frac{\partial \mathcal{L}_d}{\partial W_d} = (W_d Z + \mathbf{b}_d \mathbf{1}^T - Y) Z^T = W_d Z Z^T + \mathbf{b}_d \mathbf{1}^T Z^T - Y Z^T = 0$$

Solving for  $W_d$  we have:

$$(5.10) \quad \begin{aligned} W_d Z Z^T + \mathbf{b}_d \mathbf{1}^T Z^T - Y Z^T &= 0 \\ W_d Z Z^T + \frac{1}{n_t} (Y \mathbf{1} - W_d Z \mathbf{1}) \mathbf{1}^T Z^T - Y Z^T &= 0 \\ W_d Z Z^T - W_d Z \frac{\mathbf{1} \mathbf{1}^T}{n_t} Z^T - Y Z^T + Y \frac{\mathbf{1} \mathbf{1}^T}{n_t} Z^T &= 0 \\ W_d \bar{Z} \bar{Z}^T - \bar{Y} \bar{Z}^T &= 0 \\ W_d &= \bar{Y} \bar{Z}^\dagger \end{aligned}$$

Recall that  $Z = W_e Y + \mathbf{b}_e \mathbf{1}^T$ , then using the identities  $\bar{\mathbf{z}} = Z \frac{\mathbf{1}}{n_t}$  and  $\bar{Z} = Z - \bar{\mathbf{z}} \mathbf{1}^T$ , we have

$$(5.11) \quad \begin{aligned} \bar{\mathbf{z}} &= (W_e Y + \mathbf{b}_e \mathbf{1}^T) \mathbf{1} = W_e Y \mathbf{1} + (U \mathbf{1} - W_e Y \mathbf{1}) = \bar{\mathbf{u}} \\ \bar{Z} &= W_e \bar{Y} = \bar{U} \bar{Y}^\dagger \bar{Y} \end{aligned}$$

**Summary:** From (5.4), (5.6), (5.8), (5.10), and (5.11), the solutions for the encoder  $(W_e, \mathbf{b}_e)$  and decoder  $(W_d, \mathbf{b}_d)$  are:

$$(5.12) \quad \begin{aligned} W_e &= \bar{U} \bar{Y}^\dagger, & \mathbf{b}_e &= \frac{1}{n_t} (U \mathbf{1} - W_e Y \mathbf{1}) = \bar{\mathbf{u}} - \bar{U} \bar{Y}^\dagger \bar{\mathbf{y}} \\ W_d &= \bar{Y} \bar{Z}^\dagger = \bar{Y} (\bar{U} \bar{Y}^\dagger \bar{Y})^\dagger, & \mathbf{b}_d &= \frac{1}{n_t} (Y \mathbf{1} - W_d Z \mathbf{1}) = \bar{\mathbf{y}} - \bar{Y} (\bar{U} \bar{Y}^\dagger \bar{Y})^\dagger \bar{\mathbf{u}} \end{aligned}$$

## 5.2. Derivation of $W_e, \mathbf{b}_e, W_d, \mathbf{b}_d$ for nPOP.

For the encoder loss, we have:

$$\mathcal{L}_e = \frac{1}{2} \|W_e U + \mathbf{b}_e \mathbf{1}^T - Y\|_F^2$$

For simplicity, let's denote  $Z = W_e U + \mathbf{b}_e \mathbf{1}^T$ . Then, the loss for decoder given pretrained encoder is:

$$\mathcal{L}_d = \frac{1}{2} \|W_d Z + \mathbf{b}_d \mathbf{1}^T - U\|_F^2$$

Recall that  $Z = W_e U + \mathbf{b}_e \mathbf{1}^T$ , then using the identities  $\bar{\mathbf{z}} = Z \frac{\mathbf{1}}{n_t}$  and  $\bar{Z} = Z - \bar{\mathbf{z}} \mathbf{1}^T$ , we have

$$(5.13) \quad \begin{aligned} \bar{\mathbf{z}} &= \bar{\mathbf{u}} \\ \bar{Z} &= W_e \bar{U} = \bar{Y} \bar{U}^\dagger \bar{U} = G \bar{U} \bar{U}^\dagger \bar{U} = G \bar{U} = \bar{Y} \end{aligned}$$

**Summary:** Following the same procedure as [subsection 5.1](#), we can derive the optimal solutions for the encoder ( $W_e$ ,  $\mathbf{b}_e$ ) and decoder ( $W_d$ ,  $\mathbf{b}_d$ ) for the **nPOP** model.

(5.14)

$$\begin{aligned} W_e &= \bar{Y} \bar{U}^\dagger = G \bar{U} \bar{U}^\dagger, & \mathbf{b}_e &= \frac{1}{n_t} (Y \mathbf{1} - \bar{Y} \bar{U}^\dagger U \mathbf{1}) = \bar{\mathbf{y}} - G \bar{U} \bar{U}^\dagger \bar{\mathbf{u}} = G (I - \bar{U} \bar{U}^\dagger) \bar{\mathbf{u}} \\ W_d &= \bar{U} \bar{Z}^\dagger = \bar{U} \bar{Y}^\dagger, & \mathbf{b}_d &= \frac{1}{n_t} (U \mathbf{1} - \bar{U} \bar{Z}^\dagger Z \mathbf{1}) = \bar{\mathbf{u}} - \bar{U} \bar{Y}^\dagger \bar{\mathbf{y}} \end{aligned}$$

### 5.3. Derivation of $W_e$ , $\mathbf{b}_e$ , $W_d$ , $\mathbf{b}_d$ for **mcPOP**.

#### Loss function:

For the encoder loss, we have:

$$\mathcal{L}_e = \frac{1}{2} \|W_e U + \mathbf{b}_e \mathbf{1}^T - Y\|_F^2$$

For simplicity, let's denote  $Z = W_e U + \mathbf{b}_e \mathbf{1}^T$ . Then, the loss for decoder given pretrained encoder is:

$$\mathcal{L}_d = \frac{1}{2} \|W_d Z + \mathbf{b}_d \mathbf{1}^T - U\|_F^2 + \frac{\lambda}{2} \|G^B (W_d Z + \mathbf{b}_d \mathbf{1}^T - Y)\|_F^2$$

**Zero gradients and solving:** To find the optimal values, we set all gradients to zero and solve the resulting system of equations:

- Gradient with respect to  $\mathbf{b}_e$

$$(5.15) \quad \frac{\partial \mathcal{L}_e}{\partial \mathbf{b}_e} = (W_e U + \mathbf{b}_e \mathbf{1}^T - Y) \mathbf{1} = W_e U \mathbf{1} + n_t \mathbf{b}_e - Y \mathbf{1} = 0$$

Solving for  $\mathbf{b}_e$  we have:

$$(5.16) \quad \mathbf{b}_e = \frac{1}{n_t} (Y \mathbf{1} - W_e U \mathbf{1})$$

- Gradient with respect to  $W_e$

$$(5.17) \quad \frac{\partial \mathcal{L}_e}{\partial W_e} = (W_e U + \mathbf{b}_e \mathbf{1}^T - Y) U^T = W_e U U^T + \mathbf{b}_e \mathbf{1}^T U^T - Y U^T = 0$$

Solving for  $W_e$  we have:

$$(5.18) \quad \begin{aligned} W_e U U^T + \mathbf{b}_e \mathbf{1}^T U^T - Y U^T &= 0 \\ W_e U U^T + \frac{1}{n_t} (Y \mathbf{1} - W_e U \mathbf{1}) \mathbf{1}^T U^T - Y U^T &= 0 \\ W_e U U^T - W_e U \frac{\mathbf{1} \mathbf{1}^T}{n_t} U^T - Y U^T + Y \frac{\mathbf{1} \mathbf{1}^T}{n_t} U^T &= 0 \\ W_e \bar{U} \bar{U}^T - \bar{Y} \bar{U}^T &= 0 \\ W_e &= \bar{Y} \bar{U}^\dagger \end{aligned}$$

- Gradient with respect to  $\mathbf{b}_d$

$$(5.19) \quad \frac{\partial \mathcal{L}_d}{\partial \mathbf{b}_d} = (W_d Z + \mathbf{b}_d \mathbf{1}^T - U) \mathbf{1} + \lambda G^{B^T} (G^B (W_d Z + \mathbf{b}_d \mathbf{1}^T) - Y) \mathbf{1} = 0$$

Solving for  $\mathbf{b}_d$  we have:

$$(5.20) \quad \mathbf{b}_d = \frac{1}{n_t} (U \mathbf{1} - W_d Z \mathbf{1}) - \lambda G^{B^T} (G^B (W_d Z + \mathbf{b}_d \mathbf{1}^T) - Y) \mathbf{1}$$

- Gradient with respect to  $W_d$

$$(5.21) \quad \begin{aligned} \frac{\partial \mathcal{L}_d}{\partial W_d} &= (W_d Z + \mathbf{b}_d \mathbf{1}^T - U) Z^T + \lambda G^{B^T} (G^B (W_d Z + \mathbf{b}_d \mathbf{1}^T) - Y) Z^T = 0 \\ W_d Z Z^T + \mathbf{b}_d \mathbf{1}^T Z^T - U Z^T + \lambda G^{B^T} G^B W_d Z Z^T + \lambda G^{B^T} G^B \mathbf{b}_d \mathbf{1}^T Z^T - \lambda G^{B^T} Y Z^T &= 0 \\ (I + \lambda G^{B^T} G^B) W_d Z Z^T - (U Z^T + \lambda G^{B^T} Y Z^T) + (I + \lambda G^{B^T} G^B) \mathbf{b}_d \mathbf{1}^T Z^T &= 0 \end{aligned}$$

Solving for  $W_d$  we have:

$$(5.22) \quad \begin{aligned} (I + \lambda G^{B^T} G^B) W_d Z Z^T &= (U Z^T + \lambda G^{B^T} Y Z^T) - (I + \lambda G^{B^T} G^B) \mathbf{b}_d \mathbf{1}^T Z^T \\ (I + \lambda G^{B^T} G^B) W_d Z Z^T &= (U Z^T + \lambda G^{B^T} Y Z^T) \\ &\quad - \frac{1}{n_t} (U \mathbf{1} - W_d Z \mathbf{1} + \lambda G^{B^T} Y \mathbf{1} - \lambda G^{B^T} G^B W_d Z \mathbf{1}) \mathbf{1}^T Z^T \\ (I + \lambda G^{B^T} G^B) W_d \bar{Z} \bar{Z}^T &= \bar{U} \bar{Z}^T + \lambda G^{B^T} \bar{Y} \bar{Z}^T \\ W_d &= (I + \lambda G^{B^T} G^B)^{-1} (\bar{U} \bar{Z}^\dagger + \lambda G^{B^T} \bar{Y} \bar{Z}^\dagger) \end{aligned}$$

Recall that  $\bar{Z} = W_e \bar{U}$ , then using the identities  $\bar{z} = Z \frac{\mathbf{1}}{n_t}$  and  $\bar{Z} = Z - \bar{z} \mathbf{1}^T$ , we have

$$(5.23) \quad \begin{aligned} \bar{z} &= \bar{\mathbf{u}} \\ \bar{Z} &= W_e \bar{U} = \bar{Y} \bar{U}^\dagger \bar{U} = G^B \bar{U} \bar{U}^\dagger \bar{U} = \bar{Y} \end{aligned}$$

**Summary:** From (5.16), (5.18), (5.20), (5.22), and (5.23) we can derive the optimal solutions for the encoder  $(W_e, \mathbf{b}_e)$  and decoder  $(W_d, \mathbf{b}_d)$  for the **mcPOP** model.

$$(5.24) \quad \begin{aligned} W_e &= \bar{Y} \bar{U}^\dagger = G^B \bar{U} \bar{U}^\dagger, & \mathbf{b}_e &= \frac{1}{n_t} \left( Y \mathbf{1} - \bar{Y} \bar{U}^\dagger U \mathbf{1} \right) = \bar{\mathbf{y}} - G^B \bar{U} \bar{U}^\dagger \bar{\mathbf{u}}, \\ W_d &= (I + \lambda G^{B^T} G^B)^{-1} \left( \bar{U} \bar{Y}^\dagger + \lambda G^{B^T} \bar{Y} \bar{Y}^\dagger \right), \\ \mathbf{b}_d &= (I + \lambda G^{B^T} G^B)^{-1} \left( \bar{\mathbf{u}} + \lambda G^{B^T} \bar{\mathbf{y}} - \left( \bar{U} \bar{Y}^\dagger + \lambda G^{B^T} \bar{Y} \bar{Y}^\dagger \right) \bar{\mathbf{y}} \right) \end{aligned}$$

#### 5.4. Derivation of $W_e, \mathbf{b}_e, W_d, \mathbf{b}_d$ for **mcOPO**.

##### Loss function:

For the encoder loss, we have:

$$\mathcal{L}_e = \frac{1}{2} \|W_e Y + \mathbf{b}_e \mathbf{1}^T - U\|_F^2 + \frac{\lambda}{2} \|G^B (W_e Y + \mathbf{b}_e \mathbf{1}^T) - Y\|_F^2$$

For simplicity, let's denote  $Z = W_e Y + \mathbf{b}_e \mathbf{1}^T$ . Then, the loss for decoder given pretrained encoder is:

$$\mathcal{L}_d = \frac{1}{2} \|W_d Z + \mathbf{b}_d \mathbf{1}^T - G^B Z\|_F^2$$

**Zero gradients and solving:** To find the optimal values, we set all gradients to zero and solve the resulting system of equations:

- Gradient with respect to  $\mathbf{b}_e$

$$(5.25) \quad \begin{aligned} \frac{\partial \mathcal{L}_e}{\partial \mathbf{b}_e} &= (W_e Y + \mathbf{b}_e \mathbf{1}^T - U) \mathbf{1} + \lambda G^{B^T} (G^B (W_e Y + \mathbf{b}_e \mathbf{1}^T) - Y) \mathbf{1} = 0 \\ W_e Y \mathbf{1} + \mathbf{b}_e \mathbf{1}^T \mathbf{1} - U \mathbf{1} + \lambda G^{B^T} G^B W_e Y \mathbf{1} + \lambda G^{B^T} G^B \mathbf{b}_e \mathbf{1}^T \mathbf{1} - \lambda G^{B^T} Y \mathbf{1} &= 0 \\ \left( I + \lambda G^{B^T} G^B \right) \mathbf{b}_e n_t + W_e Y \mathbf{1} - U \mathbf{1} + \lambda G^{B^T} G^B W_e Y \mathbf{1} - \lambda G^{B^T} Y \mathbf{1} &= 0 \end{aligned}$$

Solving for  $\mathbf{b}_e$  we have:

$$(5.26) \quad \mathbf{b}_e = \frac{1}{n_t} (I + \lambda G^{B^T} G^B)^{-1} (U \mathbf{1} - W_e Y \mathbf{1} - \lambda G^{B^T} G^B W_e Y \mathbf{1} + \lambda G^{B^T} Y \mathbf{1})$$

- Gradient with respect to  $W_e$

$$(5.27) \quad \begin{aligned} \frac{\partial \mathcal{L}_e}{\partial W_e} &= (W_e Y + \mathbf{b}_e \mathbf{1}^T - U) Y^T + \lambda G^{B^T} (G^B (W_e Y + \mathbf{b}_e \mathbf{1}^T) - Y) Y^T = 0 \\ W_e Y Y^T + \mathbf{b}_e \mathbf{1}^T Y^T - U Y^T + \lambda G^{B^T} G^B W_e Y Y^T + \lambda G^{B^T} G^B \mathbf{b}_e \mathbf{1}^T Y^T - \lambda G^{B^T} Y Y^T &= 0 \\ (I + \lambda G^{B^T} G^B) W_e Y Y^T + (I + \lambda G^{B^T} G^B) \mathbf{b}_e \mathbf{1}^T Y^T - U Y^T - \lambda G^{B^T} Y Y^T &= 0 \end{aligned}$$

Solving for  $W_e$  we have:

$$(5.28) \quad \begin{aligned} (I + \lambda G^{B^T} G^B) W_e Y Y^T &= U Y^T + \lambda G^{B^T} Y Y^T \\ &\quad - \frac{1}{n_t} (U \mathbf{1} - W_e Y \mathbf{1} - \lambda G^{B^T} G^B W_e Y \mathbf{1} + \lambda G^{B^T} Y \mathbf{1}) \mathbf{1}^T Y^T \\ (I + \lambda G^{B^T} G^B) W_e \bar{Y} \bar{Y}^T &= \bar{U} \bar{Y}^T + \lambda G^{B^T} \bar{Y} \bar{Y}^T \\ W_e &= (I + \lambda G^{B^T} G^B)^{-1} (\bar{U} \bar{Y}^\dagger + \lambda G^{B^T} \bar{Y} \bar{Y}^\dagger) \end{aligned}$$

Substituting  $W_e$  back into  $\mathbf{b}_e$  we have:

$$(5.29) \quad \begin{aligned} \mathbf{b}_e &= \frac{1}{n_t} (I + \lambda G^{B^T} G^B)^{-1} (U \mathbf{1} - W_e Y \mathbf{1} - \lambda G^{B^T} G^B W_e Y \mathbf{1} + \lambda G^{B^T} Y \mathbf{1}) \\ &= \frac{1}{n_t} (I + \lambda G^{B^T} G^B)^{-1} (U \mathbf{1} - (I + \lambda G^{B^T} G^B) W_e Y \mathbf{1} + \lambda G^{B^T} Y \mathbf{1}) \\ &= (I + \lambda G^{B^T} G^B)^{-1} (U \mathbf{1} - (\bar{U} \bar{Y}^\dagger + \lambda G^{B^T} \bar{Y} \bar{Y}^\dagger) Y \mathbf{1} + \lambda G^{B^T} Y \mathbf{1}) \frac{1}{n_t} \\ &= (I + \lambda G^{B^T} G^B)^{-1} (\bar{\mathbf{u}} + \lambda G^{B^T} \bar{\mathbf{y}} - (\bar{U} \bar{Y}^\dagger + \lambda G^{B^T} \bar{Y} \bar{Y}^\dagger) \bar{\mathbf{y}}) \end{aligned}$$

- Gradient with respect to  $\mathbf{b}_d$

$$(5.30) \quad \frac{\partial \mathcal{L}_d}{\partial \mathbf{b}_d} = (W_d Z + \mathbf{b}_d \mathbf{1}^T - G^B Z) \mathbf{1} = W_d Z \mathbf{1} + \mathbf{b}_d \mathbf{1}^T \mathbf{1} - G^B Z \mathbf{1} = 0$$

Solving for  $\mathbf{b}_d$  we have:

$$(5.31) \quad \mathbf{b}_d = \frac{1}{n_t} (G^B Z \mathbf{1} - W_d Z \mathbf{1}) = G^B \bar{\mathbf{z}} - W_d \bar{\mathbf{z}}$$

- Gradient with respect to  $W_d$

$$(5.32) \quad \frac{\partial \mathcal{L}_d}{\partial W_d} = (W_d Z + \mathbf{b}_d \mathbf{1}^T - G^B Z) Z^T = W_d Z Z^T + \mathbf{b}_d \mathbf{1}^T Z^T - G^B Z Z^T = 0$$

Solving for  $W_d$  we have:

$$(5.33) \quad \begin{aligned} W_d Z Z^T + \mathbf{b}_d \mathbf{1}^T Z^T - G^B Z Z^T &= 0 \\ W_d \bar{Z} \bar{Z}^T &= G^B \bar{Z} \bar{Z}^T \\ W_d &= G^B \bar{Z} \bar{Z}^\dagger \end{aligned}$$

- Recall that

$$(5.34) \quad \begin{aligned} Z &= W_e Y + \mathbf{b}_e \mathbf{1}^T \\ &= (I + \lambda G^{B^T} G^B)^{-1} \left( (\bar{U} \bar{Y}^\dagger + \lambda G^{B^T} \bar{Y} \bar{Y}^\dagger) Y + (\bar{\mathbf{u}} + \lambda G^{B^T} \bar{\mathbf{y}} - (\bar{U} \bar{Y}^\dagger + \lambda G^{B^T} \bar{Y} \bar{Y}^\dagger) \bar{\mathbf{y}}) \mathbf{1}^T \right) \\ &= (I + \lambda G^{B^T} G^B)^{-1} \left( \bar{U} \bar{Y}^\dagger Y - \bar{U} \bar{Y}^\dagger \bar{\mathbf{y}} \mathbf{1}^T + \lambda G^{B^T} \bar{Y} \bar{Y}^\dagger Y - \lambda G^{B^T} \bar{Y} \bar{Y}^\dagger \bar{\mathbf{y}} \mathbf{1}^T + (\bar{\mathbf{u}} + \lambda G^{B^T} \bar{\mathbf{y}}) \mathbf{1}^T \right) \\ &= (I + \lambda G^{B^T} G^B)^{-1} \left( \bar{U} \bar{Y}^\dagger \bar{Y} + \lambda G^{B^T} \bar{Y} \bar{Y}^\dagger \bar{Y} + (\bar{\mathbf{u}} + \lambda G^{B^T} \bar{\mathbf{y}}) \mathbf{1}^T \right) \\ &= (I + \lambda G^{B^T} G^B)^{-1} \left( \bar{U} \bar{Y}^\dagger \bar{Y} + \lambda G^{B^T} \bar{Y} \right) + (I + \lambda G^{B^T} G^B)^{-1} \left( (\bar{\mathbf{u}} + \lambda G^{B^T} \bar{\mathbf{y}}) \mathbf{1}^T \right) \end{aligned}$$

then using the identities  $\bar{\mathbf{z}} = Z \frac{\mathbf{1}}{n_t}$  and  $\bar{Z} = Z - \bar{\mathbf{z}} \mathbf{1}^T$ , we have

$$(5.35) \quad \begin{aligned} \bar{\mathbf{z}} &= (I + \lambda G^{B^T} G^B)^{-1} (\bar{\mathbf{u}} + \lambda G^{B^T} \bar{\mathbf{y}}) \\ \bar{Z} &= (I + \lambda G^{B^T} G^B)^{-1} (\bar{U} \bar{Y}^\dagger \bar{Y} + \lambda G^{B^T} \bar{Y}) \end{aligned}$$

**Summary:** From (5.29), (5.28), (5.31), (5.33), and (5.35) we can derive the optimal solutions for the encoder ( $W_e$ ,  $\mathbf{b}_e$ ) and decoder ( $W_d$ ,  $\mathbf{b}_d$ ) for the **mcOPo** model.

$$(5.36) \quad \begin{aligned} W_e &= (I + \lambda G^{B^T} G^B)^{-1} (\bar{U} \bar{Y}^\dagger + \lambda G^{B^T} \bar{Y} \bar{Y}^\dagger), \\ \mathbf{b}_e &= (I + \lambda G^{B^T} G^B)^{-1} (\bar{\mathbf{u}} + \lambda G^{B^T} \bar{\mathbf{y}} - (\bar{U} \bar{Y}^\dagger + \lambda G^{B^T} \bar{Y} \bar{Y}^\dagger) \bar{\mathbf{y}}) \\ W_d &= G^B \bar{Z} \bar{Z}^\dagger, \quad \mathbf{b}_d = G^B (I - \bar{Z} \bar{Z}^\dagger) \bar{\mathbf{z}} \end{aligned}$$

### 5.5. Derivation of $W_e$ , $\mathbf{b}_e$ , $W_d$ , $\mathbf{b}_d$ for TAE.

#### Loss function:

The derivation is similar to the **mcOPo** in subsection 5.4, the key different is  $U = \mathbf{u}_0 \mathbf{1}^T \implies \bar{\mathbf{u}} = \mathbf{u}_0, \bar{U} = 0$ . Therefore, the optimal solutions for the encoder ( $W_e$ ,  $\mathbf{b}_e$ ) and decoder ( $W_d$ ,  $\mathbf{b}_d$ ) for the **TAE** model are:

**Summary:** From (5.29), (5.28), (5.31), (5.33), and (5.35) we can derive the optimal solutions for the encoder ( $W_e$ ,  $\mathbf{b}_e$ ) and decoder ( $W_d$ ,  $\mathbf{b}_d$ ) for the TAE model.

$$(5.37) \quad \begin{aligned} W_e &= (I + \lambda G^{B^T} G^B)^{-1} (\lambda G^{B^T} \bar{Y} \bar{Y}^\dagger), \\ \mathbf{b}_e &= (I + \lambda G^{B^T} G^B)^{-1} (\mathbf{u}_0 + \lambda G^{B^T} \bar{\mathbf{y}} - \lambda G^{B^T} \bar{Y} \bar{Y}^\dagger \bar{\mathbf{y}}) \\ W_d &= G^B \bar{Z} \bar{Z}^\dagger, \quad \mathbf{b}_d = G^B (I - \bar{Z} \bar{Z}^\dagger) \bar{\mathbf{z}} \end{aligned}$$

where

$$(5.38) \quad \begin{aligned} \bar{\mathbf{z}} &= (I + \lambda G^{B^T} G^B)^{-1} (\mathbf{u}_0 + \lambda G^{B^T} \bar{\mathbf{y}}) \\ \bar{Z} &= (I + \lambda G^{B^T} G^B)^{-1} (\lambda G^{B^T} \bar{Y}) \end{aligned}$$

### 5.6. Derivation of $W_e$ , $\mathbf{b}_e$ , $W_d$ , $\mathbf{b}_d$ for nPOP - simultaneous optimization.

We consider the optimization of the nPOP model with the encoder and decoder trained together. The combined loss function is given as:

$$\mathcal{L} = \frac{1}{2} \|W_e U + \mathbf{b}_e \mathbf{1}^T - Y\|_F^2 + \frac{\beta}{2} \|W_d (W_e U + \mathbf{b}_e \mathbf{1}^T) + \mathbf{b}_d \mathbf{1}^T - U\|_F^2$$

For simplicity, let's denote  $Z = W_e U + \mathbf{b}_e \mathbf{1}^T$ . Then our loss function becomes:

$$\mathcal{L} = \frac{1}{2} \|Z - Y\|_F^2 + \frac{\beta}{2} \|W_d Z + \mathbf{b}_d \mathbf{1}^T - U\|_F^2$$

**Zero gradients and solving** To find the optimal values, we set all gradients to zero and solve the resulting system of equations:

- Gradient with respect to  $\mathbf{b}_d$

$$(5.39) \quad \frac{\partial \mathcal{L}}{\partial \mathbf{b}_d} = (W_d Z + \mathbf{b}_d \mathbf{1}^T - U) \mathbf{1} = W_d Z \mathbf{1} + n_t \mathbf{b}_d - U \mathbf{1} = 0$$

Solving for  $\mathbf{b}_d$  we have:

$$(5.40) \quad \mathbf{b}_d = \frac{1}{n_t} (U \mathbf{1} - W_d Z \mathbf{1})$$

- Gradient with respect to  $W_d$

$$(5.41) \quad \frac{\partial \mathcal{L}}{\partial W_d} = (W_d Z + \mathbf{b}_d \mathbf{1}^T - U) Z^T = W_d Z Z^T + \mathbf{b}_d \mathbf{1}^T Z^T - U Z^T = 0$$

Solving for  $W_d$  we have:

$$\begin{aligned}
 (5.42) \quad & W_d Z Z^T + \mathbf{b}_d \mathbf{1}^T Z^T - U Z^T = 0 \\
 & W_d Z Z^T - W_d Z \frac{\mathbf{1} \mathbf{1}^T}{n_t} Z^T - U Z^T + U \frac{\mathbf{1} \mathbf{1}^T}{n_t} Z^T = 0 \\
 & W_d \bar{Z} \bar{Z}^T - \bar{U} \bar{Z}^T = 0 \\
 & W_d = \bar{U} \bar{Z}^\dagger
 \end{aligned}$$

where  $\bar{Z} = W_e \bar{U}$ . From the condition for  $W_d$ ,  $W_d \bar{Z} \bar{Z}^T - \bar{U} \bar{Z}^T = W_d W_e \bar{U} \bar{U}^T W_e^T - \bar{U} \bar{U}^T W_e^T = 0$ , then

$$(5.43) \quad W_e \bar{U} \bar{U}^T = W_e \bar{U} \bar{U}^T W_e^T W_d^T$$

we have  $W_d W_e \bar{U} \bar{U}^T W_e^T W_d^T$  is symmetric, and thus  $W_d W_e \bar{U} \bar{U}^T$  is also symmetric. In other words, we have a relationship,

$$W_d W_e \bar{U} \bar{U}^T = \bar{U} \bar{U}^T W_e^T W_d^T$$

From (5.43), we have

$$(5.44) \quad W_e \bar{U} \bar{U}^T = W_e W_d W_e \bar{U} \bar{U}^T$$

- Gradient with respect to  $\mathbf{b}_e$

$$\begin{aligned}
 (5.45) \quad & \frac{\partial \mathcal{L}}{\partial \mathbf{b}_e} = (Z - Y) \mathbf{1} + \beta [W_d^T (W_d Z + \mathbf{b}_d \mathbf{1}^T - U) \mathbf{1}] \\
 & = Z \mathbf{1} - Y \mathbf{1} + \beta [W_d^T (W_d Z + \mathbf{b}_d \mathbf{1}^T - U) \mathbf{1}] = 0
 \end{aligned}$$

Solving for  $\mathbf{b}_e$  we have:

$$\begin{aligned}
 (5.46) \quad & Z \mathbf{1} - Y \mathbf{1} + \beta [W_d^T (W_d Z + \mathbf{b}_d \mathbf{1}^T - U) \mathbf{1}] = 0 \\
 & Z \mathbf{1} - Y \mathbf{1} + \beta \left[ (\bar{U} \bar{Z}^\dagger)^T (\bar{U} \bar{Z}^\dagger) Z \mathbf{1} + n_t (\bar{U} \bar{Z}^\dagger)^T \frac{1}{n_t} (U \mathbf{1} - (\bar{U} \bar{Z}^\dagger) Z \mathbf{1}) - (\bar{U} \bar{Z}^\dagger)^T U \mathbf{1} \right] = 0 \\
 & Z \mathbf{1} - Y \mathbf{1} + \beta \left[ (\bar{U} \bar{Z}^\dagger)^T (\bar{U} \bar{Z}^\dagger) Z \mathbf{1} + (\bar{U} \bar{Z}^\dagger)^T (U \mathbf{1} - (\bar{U} \bar{Z}^\dagger) Z \mathbf{1}) - (\bar{U} \bar{Z}^\dagger)^T U \mathbf{1} \right] = 0 \\
 & Z \mathbf{1} - Y \mathbf{1} + \beta \left[ \cancel{(\bar{U} \bar{Z}^\dagger)^T (\bar{U} \bar{Z}^\dagger) Z \mathbf{1}} + \cancel{(\bar{U} \bar{Z}^\dagger)^T U \mathbf{1}} - \cancel{(\bar{U} \bar{Z}^\dagger)^T (\bar{U} \bar{Z}^\dagger) Z \mathbf{1}} - \cancel{(\bar{U} \bar{Z}^\dagger)^T U \mathbf{1}} \right] = 0 \\
 & Z \mathbf{1} - Y \mathbf{1} = 0 \\
 & W_e U \mathbf{1} + \mathbf{b}_e \mathbf{1}^T \mathbf{1} - Y \mathbf{1} = 0 \\
 & \mathbf{b}_e = \frac{1}{n_t} (Y \mathbf{1} - W_e U \mathbf{1})
 \end{aligned}$$

- Gradient with respect to  $W_e$



$$(5.47) \quad \begin{aligned} \frac{\partial \mathcal{L}}{\partial W_e} &= (Z - Y)U^T + \beta [W_d^T(W_d Z + \mathbf{b}_d \mathbf{1}^T - U)U^T] \\ &= ZU^T - YU^T + \beta [W_d^T(W_d ZU^T + \mathbf{b}_d \mathbf{1}^T U^T - UU^T)] = 0 \end{aligned}$$

We first simplify the equation:

$$(5.48) \quad \begin{aligned} ZU^T - YU^T + \beta [W_d^T(W_d ZU^T + \mathbf{b}_d \mathbf{1}^T U^T - UU^T)] &= 0 \\ W_e \bar{U} \bar{U}^T - \bar{Y} \bar{U}^T + \beta \left[ W_d^T W_d ZU^T + W_d^T \frac{1}{n_t} (U \mathbf{1} - W_d Z \mathbf{1}) \mathbf{1}^T U^T - W_d^T UU^T \right] &= 0 \\ W_e \bar{U} \bar{U}^T - \bar{Y} \bar{U}^T + \beta [W_d^T W_d \bar{Z} \bar{U}^T - W_d^T \bar{U} \bar{U}^T] &= 0 \\ W_e \bar{U} \bar{U}^T - \bar{Y} \bar{U}^T + \beta [W_d^T W_d W_e \bar{U} \bar{U}^T - W_d^T \bar{U} \bar{U}^T] &= 0 \end{aligned}$$

The best we can solve for  $W_e$  is

$$(5.49) \quad \begin{aligned} (I + \beta W_d^T W_d) W_e \bar{U} \bar{U}^T &= \bar{Y} \bar{U}^T + \beta W_d^T \bar{U} \bar{U}^T \\ W_e &= (I + \beta W_d^T W_d)^{-1} (\bar{Y} \bar{U}^T + \beta W_d^T \bar{U} \bar{U}^T) (\bar{U} \bar{U}^T)^\dagger \\ &\text{since } A^T (AA^T)^\dagger = A^\dagger, \text{ so} \\ W_e &= (I + \beta W_d^T W_d)^{-1} (G^B \bar{U} \bar{U}^\dagger + \beta W_d^T \bar{U} \bar{U}^\dagger). \end{aligned}$$

**Summary:** From (5.40), (5.42), (5.46), (5.49), we can derive the optimal solutions for the encoder ( $W_e$ ,  $\mathbf{b}_e$ ) and decoder ( $W_d$ ,  $\mathbf{b}_d$ ) for nOP0 model as training autoencoder simultaneously.

$$(5.50) \quad \begin{aligned} W_e &= (I + \beta W_d^T W_d)^{-1} (G^B \bar{U} \bar{U}^\dagger + \beta W_d^T \bar{U} \bar{U}^\dagger), & \mathbf{b}_e &= \bar{\mathbf{y}} - W_e \bar{\mathbf{u}}, \\ W_d &= \bar{U} (W_e \bar{U})^\dagger, & \mathbf{b}_d &= \bar{\mathbf{u}} - W_d \bar{\mathbf{y}}, \\ W_e \bar{U} \bar{U}^T &= W_e W_d W_e \bar{U} \bar{U}^T \end{aligned}$$